

# A partitioned scheme for fluid-composite structure interaction problems <sup>☆</sup>

M. Bukač, S. Čanić, B. Muha<sup>1</sup>

---

## Abstract

We present a loosely-coupled partitioned scheme for a benchmark problem in fluid-composite structure interaction. The benchmark problem proposed here consists of an incompressible, viscous fluid interacting with a composite structure that consists of two layers: a thin elastic layer which is in contact with the fluid, and a thick elastic layer which sits on top of the thin layer. The motivation comes from fluid-structure interaction (FSI) in hemodynamics. The equations of linear elasticity are used to model the thick structural layer, while the Koiter member/shell equations are used to model the thin structural layer which serves as fluid-structure interface with mass. An efficient, modular, operator-splitting scheme is proposed to simulate solutions to the coupled, nonlinear FSI problem. The operator splitting scheme separates the elastodynamics structure problem, from a fluid problem in which the thin structure inertia is included as a Robin-type boundary condition to achieve unconditional stability, without requiring any sub-iterations within time-steps. An energy estimate associated with unconditional stability is derived for the fully nonlinear FSI problem defined on moving domains. Two instructive numerical examples are presented to test the performance of the scheme, where it is shown numerically, that the scheme is at least first-order accurate in time. The second example reveals a new phenomenon in FSI problems: the presence of a thin fluid-structure interface with mass regularizes solutions to the full FSI problem.

*Keywords:* fluid-structure interaction, composite structure, partitioned scheme, blood flow

---

## 1. Introduction

### 1.1. Motivation

Composite materials are materials made from two or more constituent materials with different physical properties that when combined, produce a

material with characteristics different from the individual components [75]. The new material may be preferred for many reasons: common examples include materials which are stronger, lighter or less expensive when compared to traditional materials. Composite materials have been used in virtually all areas of engineering. Examples include marine structures such as boats, ships, and offshore structures, in aerospace industry such as aircraft design, in the design of wind and marine turbines, and in the design of sports' equipment such as skis and tennis raquets. They also appear everywhere in nature. Examples include bones, horns, wood, and biological tissues such as blood vessels of major human arteries. These materials are exposed to a wide spectrum of dynamic loads. In marine structures, aerospace industry, and in many biological constructs, whether natural or man-made, the dynamic loading comes from the surrounding fluid such as water, air, or blood flow. Understanding the interaction between composite materials and the surrounding fluid is important for the understanding of the normal function of the coupled fluid-structure system, as well as the detection of damage and/or pathologies in their function. Prevention of catastrophic events in engineered constructs, or the design of medical treatments to prevent further biological tissue damage, is aided by computational and experimental studies of fluid-composite structure interaction.

In problems in which the fluid and structure have comparable densities, which is the case with most biological tissues (e.g., arterial walls and blood), or in problems in which the structure density is less than the density of water, which is the case in several sandwich composite materials immersed in water [47], the exchange in energy between the fluid and structure is so significant that classical Dirichlet-Neumann loosely-coupled partitioned schemes for numerical simulation of these kinds of problems are unconditionally unstable [16, 57]. This is due to the so called added mass effect, also known as virtual mass, or hydrodynamic mass. As the structure vibrates, its mass is increased by the mass of the surrounding fluid, consequently decreasing its natural frequency. This is due to the increase of total kinetic energy of the structure and fluid from the addition of the kinetic energy of the fluid, which significantly impacts the structure vibrations when the structure is "light" relative to the fluid. A comprehensive study of these problems remains to be a challenge due to their significant energy exchange leading to strong nonlinearities in the coupled FSI problem, and due to the intrinsic multi-physics nature of the problem.

The motivation for this paper comes from fluid-structure interaction between blood flow and cardiovascular tissue. Arterial walls of major human arteries are composite materials consisting of three main layers: the intima,

media and adventitia, separated by thin elastic laminae, see Figure 1. The

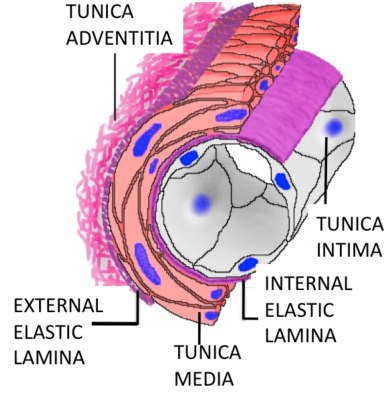


Figure 1: Arterial wall layers.

intima is the innermost, thin layer, which is mainly composed of endothelial cells. The media is the middle layer and it is mainly composed of elongated smooth muscle cells, and also elastin and collagen. The adventitia is the outermost layer, and it is mainly composed of collagen fibrils, elastic sheets and elastic fibrils. The media gives rise to the majority of the vessel's elastic (viscoelastic) behavior.

Arterial walls interact with blood flow. This interaction plays a crucial role in the normal physiology and pathophysiology of the human cardiovascular system. During systole, when the left ventricle of the heart contracts and squeezes blood to the aorta, the kinetic energy imparted by blood to the aortic walls stretches the walls outward. Once the artery is distended with blood, energy stored by stretching elastic fibers is released through elastic recoil. Elastic recoil takes place during the diastolic part of cardiac cycle, when the heart's left ventricle relaxes and gets refilled with blood. During that time the elastic recoil of arteries helps propel blood to the far most parts of the cardiovascular system.

In medium-to-large human arteries, such as the aorta or coronary arteries, blood can be modeled as an incompressible, viscous, Newtonian fluid. Due to the fact that density of blood is comparable to that of arterial wall tissue, the corresponding fluid-structure interaction problem suffers from the added mass effect, discussed above. Except for the Immersed Boundary Method approaches, to this date, there have been no FSI numerical solvers based on the Arbitrary Lagrangian-Eulerian approaches, that would take into account the multi-layered structure of arterial walls, and the full non-linear (two-way) coupling with blood flow. In this manuscript we take a

first step in this direction by proposing to study a benchmark problem in fluid-multi-layered-structure interaction in which the structure consists of two layers, a thin and a thick layer, where the thin layer serves as fluid-structure interface with mass. The thin layer is modeled by the cylindrical Koiter membrane equations, while the thick layer by the equations of linear elasticity. The proposed problem is a nonlinear moving-boundary problem of parabolic-hyperbolic type.

Our computational method is based on an operator-splitting approach, introduced in [63] to study the existence of solutions to an associated fluid-multi-layered structure interaction problem. The particular Lie operator splitting used in [63] gives rise to a modular scheme that deals efficiently and elegantly with the added mass effect problem. In this scheme, the time discretization is performed via Lie operator splitting. At each time step, the full FSI problem is split into a fluid and a structure sub-problem. To deal with the motion of the fluid domain, the Arbitrary Lagrangian Eulerian (ALE) approach is adopted. To achieve stability and convergence, the splitting is performed in a special way in which the fluid sub-problem includes the thin structure inertia via a "Robin-type" boundary condition. The fact that the thin structure inertia is included implicitly in the fluid sub-problem, gives rise to the appropriate energy estimates for the approximate solutions, independent of the size of the time discretization, that provide unconditional stability of the underlying scheme [63].

In this manuscript, the proposed numerical scheme is implemented to solve two instructive numerical examples. The first example shows that the scheme recovers an exact solution to a simplified FSI problem. The second example considers a full FSI problem with a thin and thick structural layer. Since there are no numerical results in literature on FSI problems with multiple structural layers against which the numerical solution could be tested, the following strategy was used to test the solver. A sequence of solutions to FSI problems with a thin and thick structure was considered in which the thickness of the thin structure  $h$  converges to zero, while the combined thickness of the composite structure remains constant. Using analytical methods, it is shown in this manuscript that the limiting solution as  $h \rightarrow 0$  solves the FSI problem with a single, thick structural layer. The solution of the limiting problem is then numerically tested against the solution of the FSI problem with the thick structural layer, which is obtained using a different solver, published in [14], and previously tested against a monolithic solver. It is then shown that the two solutions, obtained with two different solvers, are in good agreement. In this example it is also shown numerically that the proposed operator-splitting scheme is first-order accurate in time.

Although the benchmark problem and numerical examples in this manuscript are given in 2D, there is nothing in the methodology that depends on the spatial dimension. Therefore, the methodology presented in this manuscript can be applied to 3D FSI problems. An application of the splitting to a problem in 3D can be found in [60], where a FSI with a single thin structure was considered.

We also emphasize that the same (equivalent) splitting strategy can be applied to problems in which the composite structure is viscoelastic. Such a splitting was presented, for example, in [11], where a single, thin viscoelastic Koiter shell was coupled to the motion of the fluid. See also [14] for a corresponding FSI problem involving a thick viscoelastic structure. Since structural viscosity further stabilizes the underlying FSI problem, in this manuscript we consider the most “difficult” case, namely the case when the composite structure is purely elastic.

The work presented in this manuscript reveals a new phenomenon which is related to the smoothing effects provided by the purely elastic fluid-structure interface *with mass*. Our simulations show that the presence of a thin fluid-structure interface with mass regularizes solutions of the entire FSI problem. Our results in the companion paper on the analysis (existence) of solutions to fluid-multi-layered structure interaction problem [63] show that the *inertia* of the thin fluid-structure interface with mass provides higher regularity of the coupled problem. This is reminiscent of the results by Hansen and Zuazua [40] in which the presence of point mass at the interface between two linearly elastic strings with solutions in asymmetric spaces (different regularity on each side) allowed the proof of well-posedness due to the regularizing effects by the point mass. Based on the computational results presented in example 2 of this manuscript, we conclude that the fluid-structure interface inertia regularizes the motion of the fluid-structure interface, and acts as a regularizing mechanism for the entire solution of this FSI problem.

### 1.2. Description of the fluid-structure interaction problem

We consider the flow of an incompressible, viscous fluid in a two-dimensional channel of reference length  $L$ , and reference width  $2R$ , see Figure 2. The channel is bounded by a deformable wall, which is composed of two layers: a thin elastic layer with thickness  $h$ , and a thick elastic layer with thickness  $H$ . The thin layer serves as fluid-structure interface with mass.

We are interested in simulating a pressure-driven flow through the deformable 2D channel with two-way coupling between the fluid and structure. The structure deforms because of the fluid loading onto the structure, while

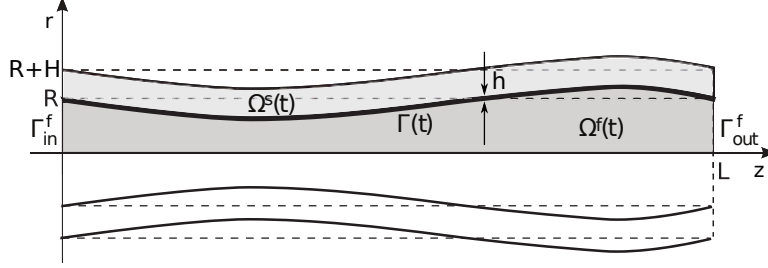


Figure 2: Deformed domains  $\Omega^f(t) \cup \Omega^s(t)$ .

at the same time, the fluid flow and the fluid domain are affected by the elastodynamics of the structure. Deformation of the structure will be given with respect of a reference configuration, i.e., in Lagrangian framework, where the reference structural domain is assumed to be a uniform cylindrical annulus with constant radius and thickness. Without loss of generality, we consider only the upper half of the fluid domain supplemented by a symmetry condition at the axis of symmetry. Thus, the reference fluid and structure domains in our problem are given, respectively, by

$$\begin{aligned}\hat{\Omega}^f &:= \{(z, r) | 0 < z < L, 0 < r < R\}, \\ \hat{\Omega}^s &:= \{(z, r) | 0 < z < L, R < r < R + H\}.\end{aligned}$$

Here  $z$  and  $r$  denote the horizontal and vertical Cartesian coordinates, respectively (see Figure 2). The reference configuration of the fluid-structure interface is given by

$$\hat{\Gamma} := \{(z, R) | 0 < z < L\}.$$

The flow of an incompressible, viscous fluid is modeled by the Navier-Stokes equations:

$$\rho_f \left( \frac{\partial \mathbf{v}}{\partial t} + \mathbf{v} \cdot \nabla \mathbf{v} \right) = \nabla \cdot \boldsymbol{\sigma}^f(\mathbf{v}, p) \quad \text{in } \Omega^f(t) \times (0, T), \quad (1)$$

$$\nabla \cdot \mathbf{v} = 0 \quad \text{in } \Omega^f(t) \times (0, T), \quad (2)$$

where  $\mathbf{v} = (v_z, v_r)$  is the fluid velocity,  $p$  is the fluid pressure,  $\rho_f$  is fluid density, and  $\boldsymbol{\sigma}^f$  is the fluid stress tensor. For a Newtonian fluid the stress tensor is given by  $\boldsymbol{\sigma}^f(\mathbf{v}, p) = -p\mathbf{I} + 2\mu_f \mathbf{D}(\mathbf{v})$ , where  $\mu_f$  is the fluid viscosity and  $\mathbf{D}(\mathbf{v}) = (\nabla \mathbf{v} + (\nabla \mathbf{v})^\tau)/2$  is the rate-of-strain tensor.

The inlet to the fluid domain will be denoted by  $\Gamma_{in}^f = \{0\} \times (0, R)$ , and the outlet by  $\Gamma_{out}^f = \{L\} \times (0, R)$ . The flow will be driven by the inlet and

outlet “pressure” data. Two sets of inlet and outlet boundary conditions will be considered.

**BC1.** The *normal stress* inlet and outlet data:

$$\boldsymbol{\sigma} \mathbf{n}_{in/out}^f = -p_{in/out}(t) \mathbf{n}_{in/out}^f \text{ on } \Gamma_{in/out}^f \times (0, T), \quad (3)$$

where  $\mathbf{n}_{in}^f$  and  $\mathbf{n}_{out}^f$  are the corresponding outward unit normals. Even though not physiologically optimal, these boundary conditions are common in blood flow simulations [4, 59, 65].

**BC2.** The *dynamic pressure* inlet and outlet data:

$$\left. \begin{aligned} p + \frac{\rho_f}{2} |u|^2 &= p_{in/out}(t) \\ u_r &= 0 \end{aligned} \right\} \text{ on } \Gamma_{in/out}^f \times (0, T), \quad (4)$$

where  $p_{in/out} \in L_{loc}^2(0, \infty)$  are given. Therefore, the fluid flow is driven by a prescribed dynamic pressure drop, and the flow enters and leaves the fluid domain orthogonally to the inlet and outlet boundary. This set of boundary conditions will be used in energy estimates and in the proof of stability of the proposed scheme.

At the bottom fluid boundary denoted by  $\Gamma_b$ , defined by  $(0, L) \times \{0\}$ , the following symmetry conditions are prescribed:

$$\frac{\partial v_z}{\partial r}(z, 0, t) = 0, \quad v_r(z, 0, t) = 0 \quad \text{on } (0, L) \times (0, T). \quad (5)$$

The lateral fluid boundary is bounded by a deformable, composite structure. The thin layer, which is in contact with the fluid, is modeled by the linearly elastic Koiter membrane model:

$$\rho_m h \frac{\partial^2 \hat{\eta}_z}{\partial t^2} - C_2 \frac{\partial \hat{\eta}_r}{\partial \hat{z}} - C_1 \frac{\partial^2 \hat{\eta}_z}{\partial \hat{z}^2} = \hat{f}_z \quad \text{on } \hat{\Gamma} \times (0, T), \quad (6)$$

$$\rho_m h \frac{\partial^2 \hat{\eta}_r}{\partial t^2} + C_0 \hat{\eta}_r + C_2 \frac{\partial \hat{\eta}_z}{\partial \hat{z}} = \hat{f}_r \quad \text{on } \hat{\Gamma} \times (0, T), \quad (7)$$

where  $\hat{\boldsymbol{\eta}}(\hat{z}, t) = (\hat{\eta}_z(\hat{z}, t), \hat{\eta}_r(\hat{z}, t))$  denotes the axial and radial components of displacement,  $\hat{\mathbf{f}} = (\hat{f}_z, \hat{f}_r)$  is the surface density of the force applied to the shell,  $\rho_m$  denotes membrane density, and

$$C_0 = \frac{h}{R^2} \left( \frac{2\mu_m \lambda_m}{\lambda_m + 2\mu_m} + 2\mu_m \right), \quad C_1 = h \left( \frac{2\mu_m \lambda_m}{\lambda_m + 2\mu_m} + 2\mu_m \right), \quad C_2 = \frac{h}{R} \frac{2\mu_m \lambda_m}{\lambda_m + 2\mu_m}, \quad (8)$$

where  $\mu_m$  and  $\lambda_m$  are the Lamé constants. In terms of the Young's modulus of elasticity and Poisson ratio, coefficients  $C_0$ ,  $C_1$ , and  $C_2$  can be written as

$$C_0 = \frac{hE}{R^2(1-\sigma^2)}, \quad C_1 = \frac{hE}{1-\sigma^2}, \quad C_2 = \frac{hE\sigma}{R(1-\sigma^2)}.$$

The thick layer of the wall will be modeled by the equations of linear elasticity with an added extra term  $\gamma\hat{\mathbf{U}}$ , where  $\hat{\mathbf{U}}$  denotes the thick structure displacement, to account for circumferential strain whose effects are lost in the transition from 3D to 2D [7, 5, 55, 8]. This term corresponds to the non-differentiated term in the Koiter membrane equations (7) containing the coefficient  $C_0$ , which appears in these equations due to the cylindrical geometry of the domain. If the structure is not fixed at the end points, this term helps keep the top and bottom portions of the structure domain together. The model reads:

$$\rho_s \frac{\partial^2 \hat{\mathbf{U}}}{\partial t^2} + \gamma \hat{\mathbf{U}} = \nabla \cdot \boldsymbol{\sigma}^s(\hat{\mathbf{U}}) \quad \text{in } \hat{\Omega}^s \times (0, T), \quad (9)$$

where  $\hat{\mathbf{U}} = (\hat{U}_z, \hat{U}_r)$  is the structure displacement and  $\rho_s$  is the structure density. We will be assuming that the thick structure behaves as a linearly elastic Saint-Venant Kirchhoff material, in which case the stress-displacement relationship is given by

$$\boldsymbol{\sigma}^s(\hat{\mathbf{U}}) = 2\mu_s \mathbf{D}(\hat{\mathbf{U}}) + \lambda_s (\nabla \cdot \hat{\mathbf{U}}) \mathbf{I},$$

where  $\mu_s$  and  $\lambda_s$  are the Lamé coefficients for the thick layer. In the simulations presented in Sections 5 and 6 the Lamé constants of the thin and thick structural layer will be assumed to be the same:

$$\lambda_m = \lambda_s, \quad \mu_m = \mu_s.$$

The thick structure will be assumed to be fixed at the inlet and outlet boundaries:

$$\hat{\mathbf{U}}(0, r, t) = \hat{\mathbf{U}}(L, r, t) = 0 \quad \text{on } [R, R+H] \times (0, T). \quad (10)$$

Furthermore, at the external structure boundary  $\hat{\Gamma}_{ext}^s = \{R+H\} \times (0, L)$  the structure will be exposed to zero external ambient pressure, while the axial displacement remains fixed:

$$\mathbf{n}_{ext}^s \cdot \boldsymbol{\sigma}^s \mathbf{n}_{ext}^s = 0 \quad \text{on } \hat{\Gamma}_{ext}^s \times (0, T), \quad (11)$$

$$\hat{U}_z = 0 \quad \text{on } \hat{\Gamma}_{ext}^s \times (0, T), \quad (12)$$



where  $\mathbf{n}_{ext}^s$  is the outward unit normal vector on  $\hat{\Gamma}_{ext}^s$ .

Initially, the fluid and the structure are assumed to be at rest, with zero displacement from the reference configuration

$$\mathbf{v} = 0, \quad \hat{\boldsymbol{\eta}} = 0, \quad \frac{\partial \hat{\boldsymbol{\eta}}}{\partial t} = 0, \quad \hat{\mathbf{U}} = 0, \quad \frac{\partial \hat{\mathbf{U}}}{\partial t} = 0, \quad \text{at } t = 0. \quad (13)$$

The fluid and the composite structure are coupled via the following kinematic and dynamic boundary conditions [73, 58]:

- **Kinematic coupling conditions** describe continuity of velocity at the fluid-structure interface (no-slip)

$$\mathbf{v}(\hat{z} + \hat{\eta}_z(\hat{z}, t), R + \hat{\eta}_r(\hat{z}, t), t) = \frac{\partial \hat{\boldsymbol{\eta}}}{\partial t}(\hat{z}, t) \quad \text{on } (0, L) \times (0, T), \quad (14)$$

and continuity of displacement

$$\hat{\boldsymbol{\eta}}(\hat{z}, t) = \hat{\mathbf{U}}(\hat{z}, R, t) \quad \text{on } (0, L) \times (0, T); \quad (15)$$

- **Dynamic coupling condition** describes the second Newton's law of motion of the fluid-structure interface, which is loaded by the normal stresses exerted by both the fluid and thick structure. The condition reads:

$$\begin{pmatrix} \rho_m h \frac{\partial^2 \hat{\eta}_z}{\partial t^2} - C_2 \frac{\partial \hat{\eta}_r}{\partial \hat{z}} - C_1 \frac{\partial^2 \hat{\eta}_z}{\partial \hat{z}^2} \\ \rho_m h \frac{\partial^2 \hat{\eta}_r}{\partial t^2} + C_0 \hat{\eta}_r + C_2 \frac{\partial \hat{\eta}_z}{\partial \hat{z}} \end{pmatrix} = J \widehat{\boldsymbol{\sigma}^f \mathbf{n}^f}|_{\Gamma(t)} + \boldsymbol{\sigma}^s \mathbf{n}^s|_{\hat{\Gamma}}, \quad (16)$$

on  $(0, L) \times (0, T)$ , where  $J$  denotes the Jacobian of the transformation from Eulerian to Lagrangian coordinates, and  $\widehat{\boldsymbol{\sigma}^f \mathbf{n}^f}|_{\Gamma(t)}$  denotes the normal fluid stress at the deformed fluid-structure interface, evaluated on the reference configuration, namely at the points  $(\hat{z} + \hat{\eta}_z(\hat{z}, t), R + \hat{\eta}_r(\hat{z}, t))$  for  $\hat{z} \in (0, L)$  and  $t \in (0, T)$ . Vector  $\mathbf{n}^f$  is the outward unit normal to the deformed fluid domain, and  $\mathbf{n}^s$  is the outward unit normal to the structure domain.

### 1.3. The energy of the coupled problem

The coupled fluid-composite structure interaction problem (1)-(16) with dynamic pressure inlet and outlet data, satisfies the following energy equal-

ity:

$$\begin{aligned}
& \frac{d}{dt} \left\{ \underbrace{\frac{\rho_f}{2} \|\mathbf{v}\|_{L^2(\Omega^f(t))}^2 + \frac{\rho_m h}{2} \left\| \frac{\partial \hat{\eta}_z}{\partial t} \right\|_{L^2(0,L)}^2 + \frac{\rho_m h}{2} \left\| \frac{\partial \hat{\eta}_r}{\partial t} \right\|_{L^2(0,L)}^2 + \frac{\rho_s}{2} \left\| \frac{\partial \hat{\mathbf{U}}}{\partial t} \right\|_{L^2(\hat{\Omega}^s)}^2}_{\text{Kinetic Energy of the Coupled Problem}} \right. \\
& \quad + h \left[ 4\mu_m \left\| \frac{\hat{\eta}_r}{R} \right\|_{L^2(0,L)}^2 + 4\mu_m \left\| \frac{\partial \hat{\eta}_z}{\partial \hat{z}} \right\|_{L^2(0,L)}^2 + \frac{4\mu_m \lambda_m}{\lambda_m + 2\mu_m} \left\| \frac{\partial \hat{\eta}_z}{\partial \hat{z}} + \frac{\hat{\eta}_r}{R} \right\|_{L^2(0,L)}^2 \right] \\
& \quad \underbrace{\left. + \frac{\gamma}{2} \|\hat{\mathbf{U}}\|_{L^2(\hat{\Omega}^s)}^2 + \mu_s \|\mathbf{D}(\hat{\mathbf{U}})\|_{L^2(\hat{\Omega}^s)}^2 + \frac{\lambda_s}{2} \|\nabla \cdot \hat{\mathbf{U}}\|_{L^2(\hat{\Omega}^s)}^2 \right\}_{\text{Thick Structure Elastic Energy}} \\
& \quad + \underbrace{2\mu_f \|\mathbf{D}(\mathbf{v})\|_{L^2(\Omega^f(t))}^2}_{\text{Fluid Viscous Energy}} = \int_0^R p_{in}(t) v_z|_{z=0} dr - \int_0^R p_{out}(t) v_z|_{z=L} dr. \quad (17)
\end{aligned}$$

The derivation of the energy equality above is similar to that in [63] where the proof of existence of a weak solution to the coupled problem was proved. The only difference with the energy obtained in [63] is that the Koiter membrane model in the current manuscript includes both the longitudinal and radial components of displacement. In this case, the total energy associated with the Koiter membrane elastodynamics is given by

$$\begin{aligned}
& \frac{d}{dt} \left( \frac{\rho_m h}{2} \left\| \frac{\partial \hat{\eta}_z}{\partial t} \right\|_{L^2(0,L)}^2 + h \left[ 4\mu_m \left\| \frac{\hat{\eta}_r}{R} \right\|_{L^2(0,L)}^2 + 4\mu_m \left\| \frac{\partial \hat{\eta}_z}{\partial \hat{z}} \right\|_{L^2(0,L)}^2 \right. \right. \\
& \quad \left. \left. + \frac{4\mu_m \lambda_m}{\lambda_m + 2\mu_m} \left\| \frac{\partial \hat{\eta}_z}{\partial \hat{z}} + \frac{\hat{\eta}_r}{R} \right\|_{L^2(0,L)}^2 \right] \right) = \int_0^L \hat{\mathbf{f}} \cdot \frac{\partial \hat{\boldsymbol{\eta}}}{\partial t} d\hat{z}. \quad (18)
\end{aligned}$$

Equation (18) is obtained after multiplying (using the dot-product) the Koiter membrane equations (6), (7) by the structure velocity  $\partial \hat{\boldsymbol{\eta}} / \partial t$  and integrating the resulting equation by parts. Similarly, the energy associated with the thick structure problem is given by

$$\begin{aligned}
& \frac{1}{2} \frac{d}{dt} \left( \rho_s \left\| \frac{\partial \hat{\mathbf{U}}}{\partial t} \right\|_{L^2(\hat{\Omega}_S)}^2 + 2\mu_s \|\mathbf{D}(\hat{\mathbf{U}})\|_{L^2(\hat{\Omega}_S)}^2 + \lambda_s \|\nabla \cdot \hat{\mathbf{U}}\|_{L^2(\hat{\Omega}_S)}^2 \right. \\
& \quad \left. + \gamma \|\hat{\mathbf{U}}\|_{L^2(\hat{\Omega}_S)}^2 \right) = - \int_0^L \boldsymbol{\sigma}^s \mathbf{e}_r \cdot \frac{\partial \hat{\mathbf{U}}}{\partial t}, \quad (19)
\end{aligned}$$

which is obtained after multiplying the thick structure problem (9) by structure velocity  $\partial \hat{\mathbf{U}} / \partial t$  and integrating the resulting equation by parts.

To deal with the fluid equations we use the same approach: multiply the momentum equation (1) by the fluid velocity and integrate by parts, using the incompressibility condition on the way, and the following identities:

$$\int_{\Omega^f(t)} \frac{\partial \mathbf{v}}{\partial t} \cdot \mathbf{v} d\mathbf{x} = \frac{1}{2} \frac{d}{dt} \int_{\Omega^f(t)} |\mathbf{v}|^2 d\mathbf{x} - \frac{1}{2} \int_{\Gamma(t)} |\mathbf{v}|^2 \mathbf{v} \cdot \mathbf{n}^f dS, \quad (20)$$

$$\int_{\Omega^f(t)} (\mathbf{v} \cdot \nabla) \mathbf{v} \cdot \mathbf{v} d\mathbf{x} = \frac{1}{2} \int_{\partial\Omega^f(t)} |\mathbf{v}|^2 \mathbf{v} \cdot \mathbf{n}^f dS, \quad (21)$$

The first identity is just the transport theorem, while the second one is obtained using integration by parts. In (21), the boundary integral over  $\partial\Omega^f(t) = \Gamma_b \cup \Gamma(t) \cup \Gamma_{in/out}$  is simplified as follows. The portion corresponding to  $\Gamma_b$  is zero due to the symmetry boundary condition, which implies  $\mathbf{v} \cdot \mathbf{n} = 0$  on  $\Gamma_b$ . The portion corresponding to  $\Gamma(t)$  is canceled with the same term appearing in the transport formula (20). Finally, the boundary terms on  $\Gamma_{in/out}$  are absorbed by the dynamic pressure boundary conditions. Therefore, after multiplying (1) with  $\mathbf{v}$ , integrating by parts and taking into account the preceding discussion, we get:

$$\begin{aligned} & \frac{\rho_f}{2} \frac{d}{dt} \|\mathbf{v}\|_{L^2(\Omega^f(t))}^2 + 2\mu_f \|\mathbf{D}(\mathbf{v})\|_{L^2(\Omega(t))}^2 - \int_{\Gamma(t)} \boldsymbol{\sigma} \mathbf{n}^f \cdot \mathbf{v} dS \\ &= - \int_0^R p_{in}(t) v_z|_{z=0} dr + \int_0^R p_{out}(t) v_z|_{z=L} dr. \end{aligned} \quad (22)$$

The energy of the Koiter shell, given by (18), the energy of the thick structure, given by (19), and the energy of the fluid, given by (22), are combined into the total energy of the coupled problem by employing the dynamic and kinematic coupling conditions. To do this, first the fluid normal stress term in (22) is written in Lagrangian coordinates as follows:

$$\int_{\Gamma(t)} \boldsymbol{\sigma} \mathbf{n}^f \cdot \mathbf{v} dS = \int_{\hat{\Gamma}} \widehat{\boldsymbol{\sigma} \mathbf{n}^f} \cdot \hat{\mathbf{v}} J d\hat{z}, \quad (23)$$

where  $J$  is the Jacobian of the transformation from Eulerian to Lagrangian coordinates. From the kinematic and dynamic coupling conditions, the normal stress term is equal to:

$$\int_{\hat{\Gamma}} \widehat{\boldsymbol{\sigma} \mathbf{n}^f} \cdot \hat{\mathbf{v}} J d\hat{z} = - \int_{\hat{\Gamma}} \hat{\mathbf{f}} \cdot \frac{\partial \hat{\boldsymbol{\eta}}}{\partial t} d\hat{z} - \int_{\hat{\Gamma}} \boldsymbol{\sigma}^s \mathbf{n}^s \cdot \frac{\partial \mathbf{U}}{\partial t} \Big|_{\hat{\Gamma}} d\hat{z}. \quad (24)$$

This is used in the final step in which the three expressions for the energy of each separate physics sub-problem (18), (19), and (22), are added together,

to obtain exactly the energy equality (17) of the coupled multi-physics FSI problem (1) - (16) driven by the time-dependent dynamic pressure data.

Therefore, we have shown that if a smooth solution to the coupled fluid-structure interaction problem (1) - (16) exists, then it satisfies the energy equality (17). This equality states that the rate of change of the kinetic energy of the fluid, the kinetic energy of the multilayered structure, and the elastic energy of the structure, plus the viscous dissipation of the fluid, is counter-balanced by the work done by the inlet and outlet data.

#### 1.4. The ALE framework

To circumvent the difficulty associated with the fact that fluid domain changes in time we adopt the Arbitrary Lagrangian Eulerian (ALE) method [42, 20, 65]. The ALE approach is based on introducing a family of arbitrary, smooth, homeomorphic mappings  $\mathcal{A}_t$  defined on the reference domain  $\hat{\Omega}^f$  such that, for each  $t \in (t_0, T)$ ,  $\mathcal{A}_t$  maps the reference domain  $\hat{\Omega}^f$  into the current domain  $\Omega^f(t)$ :

$$\mathcal{A}_t : \hat{\Omega}^f \rightarrow \Omega^f(t) \subset \mathbb{R}^2, \quad \mathbf{x} = \mathcal{A}_t(\hat{\mathbf{x}}) \in \Omega^f(t), \quad \text{for } \hat{\mathbf{x}} \in \hat{\Omega}^f.$$

We will use the ALE mapping to deal with the deformation of the mesh, and to resolve the issues related to the approximation of the time-derivative  $\partial \mathbf{v} / \partial t \approx (\mathbf{v}(t^{n+1}) - \mathbf{v}(t^n)) / \Delta t$ , which is not well-defined due to the fact that  $\Omega^f(t)$  depends on time. To rewrite the Navier-Stokes equations (1) in the ALE framework we employ the ALE mapping  $\mathcal{A}_t$  to relate a function  $f = f(\mathbf{x}, t)$  defined on  $\Omega^f(t) \times (0, T)$  to the corresponding function  $\hat{f} := f \circ \mathcal{A}_t$  defined on  $\hat{\Omega} \times (0, T)$  as

$$\hat{f}(\hat{\mathbf{x}}, t) = f(\mathcal{A}_t(\hat{\mathbf{x}}), t).$$

Differentiating the latter equation with respect to time, we have

$$\left. \frac{\partial f}{\partial t} \right|_{\hat{\mathbf{x}}} = \frac{\partial f}{\partial t} + \mathbf{w} \cdot \nabla f, \quad (25)$$

where  $\mathbf{w} = \frac{\partial \mathcal{A}_t(\hat{\mathbf{x}})}{\partial t}$  denotes the domain velocity. Note that  $\left. \frac{\partial f}{\partial t} \right|_{\hat{\mathbf{x}}}$  denotes the time derivative of  $f$  evaluated on the reference domain.

Finally, system (1)-(2) in the ALE framework reads as follows: Find  $\mathbf{v} = (v_z, v_r)$  and  $p$ , with  $\hat{\mathbf{v}}(\hat{\mathbf{x}}, t) = \mathbf{v}(\mathcal{A}_t(\hat{\mathbf{x}}), t)$  such that

$$\rho_f \left( \left. \frac{\partial \mathbf{v}}{\partial t} \right|_{\hat{\mathbf{x}}} + (\mathbf{v} - \mathbf{w}) \cdot \nabla \mathbf{v} \right) = \nabla \cdot \boldsymbol{\sigma}^f(\mathbf{v}, p), \quad \text{in } \Omega^f(t) \times (0, T), \quad (26)$$

$$\nabla \cdot \mathbf{v} = 0 \quad \text{in } \Omega^f(t) \times (0, T), \quad (27)$$

with corresponding initial and boundary conditions.

### 1.5. Weak formulation of the coupled FSI problem

For all  $t \in [0, T]$  define the following test function spaces

$$\begin{aligned} V^f(t) &= \{\varphi : \Omega^f(t) \rightarrow \mathbb{R}^2 \mid \varphi = \hat{\varphi} \circ (\mathcal{A}_t)^{-1}, \hat{\varphi} \in (H^1(\hat{\Omega}^f))^2, \\ &\quad \varphi_r|_{r=0} = 0, \varphi|_{z=0,L} = 0\}, \end{aligned} \quad (28)$$

$$Q(t) = \{q : \Omega^f(t) \rightarrow \mathbb{R} \mid q = \hat{q} \circ (\mathcal{A}_t)^{-1}, \hat{q} \in L^2(\hat{\Omega}^f)\}, \quad (29)$$

$$\hat{V}^m = \{\hat{\zeta} : (0, L) \rightarrow \mathbb{R}^2 \mid \hat{\zeta} \in (H_0^1(\hat{\Gamma}))^2\}, \quad (30)$$

$$\hat{V}^s = \{\hat{\psi} : \hat{\Omega}^s \rightarrow \mathbb{R}^2 \mid \hat{\psi} \in (H^1(\hat{\Omega}^s))^2, \hat{\psi}|_{z=0,L} = 0, \hat{\psi}_z|_{\hat{\Gamma}_{ext}^s} = 0\}, \quad (31)$$

and introduce the function space

$$V^{fsi} = \{(\varphi, \hat{\zeta}, \hat{\psi}) \in V^f(t) \times \hat{V}^m \times \hat{V}^s \mid \varphi|_{\Gamma(t)} = \zeta, \hat{\zeta} = \hat{\psi}|_{\hat{\Gamma}}\}, \quad (32)$$

where  $\zeta := \hat{\zeta} \circ (\mathcal{A}_t^{-1}|_{\Gamma(t)})$ . The variational formulation of the coupled fluid-structure interaction problem now reads: given  $t \in (0, T)$ , find  $(\mathbf{v}, \hat{\eta}, \hat{\mathbf{U}}, p) \in V^f(t) \times \hat{V}^m \times \hat{V}^s \times Q(t)$  such that (14) and (15) hold and such that for all  $(\varphi, \hat{\zeta}, \hat{\psi}, q) \in V^{fsi} \times Q(t)$

$$\begin{aligned} &\rho_f \int_{\Omega^f(t)} \frac{\partial \mathbf{v}}{\partial t} \cdot \varphi d\mathbf{x} + \int_{\Omega^f(t)} (\mathbf{v} \cdot \nabla) \mathbf{v} \cdot \varphi d\mathbf{x} + 2\mu_f \int_{\Omega^f(t)} \mathbf{D}(\mathbf{v}) : \mathbf{D}(\varphi) d\mathbf{x} \\ &- \int_{\Omega^f(t)} p \nabla \cdot \varphi d\mathbf{x} + \int_{\Omega^f(t)} q \nabla \cdot \mathbf{v} d\mathbf{x} + \rho_m h \int_0^L \frac{\partial^2 \hat{\eta}_z}{\partial t^2} \hat{\zeta}_z d\hat{z} + \rho_m h \int_0^L \frac{\partial^2 \hat{\eta}_r}{\partial t^2} \hat{\zeta}_r d\hat{z} \\ &- C_2 \int_0^L \frac{\partial \hat{\eta}_r}{\partial \hat{z}} \hat{\zeta}_z d\hat{z} + C_1 \int_0^L \frac{\partial \hat{\eta}_z}{\partial \hat{z}} \frac{\partial \hat{\zeta}_z}{\partial \hat{z}} d\hat{z} + C_0 \int_0^L \hat{\eta}_r \hat{\zeta}_r d\hat{z} + C_2 \int_0^L \frac{\partial \hat{\eta}_z}{\partial \hat{z}} \hat{\zeta}_r d\hat{z} \\ &+ \rho_s \int_{\hat{\Omega}^s} \frac{\partial^2 \hat{\mathbf{U}}}{\partial t^2} \cdot \hat{\psi} d\hat{\mathbf{x}} + 2\mu_s \int_{\hat{\Omega}^s} \mathbf{D}(\hat{\mathbf{U}}) : \mathbf{D}(\hat{\psi}) d\hat{\mathbf{x}} + \lambda_s \int_{\hat{\Omega}^s} (\nabla \cdot \hat{\mathbf{U}})(\nabla \cdot \hat{\psi}) d\hat{\mathbf{x}} \\ &+ \gamma \int_{\hat{\Omega}^s} \hat{\mathbf{U}} \cdot \hat{\psi} d\hat{\mathbf{x}} = \int_0^R p_{in}(t) \varphi_z|_{z=0} dr - \int_0^R p_{out}(t) \varphi_z|_{z=L} dr, \end{aligned} \quad (33)$$

supplemented with initial conditions.

### 1.6. Literature review

The development of numerical solvers for fluid-structure interaction problems has become particularly active since the 1980's [67, 68, 23, 31, 52, 48, 36, 35, 38, 37, 20, 42, 41, 49, 51, 70, 69, 3, 72, 21, 24, 45, 46, 17, 30].

Until recently, only monolithic algorithms seemed applicable to blood flow simulations [30, 33, 66, 77, 9, 10]. These algorithms are based on solving the entire nonlinear coupled problem as one monolithic system. They

are, however, generally quite expensive in terms of computational time, programming time and memory requirements, since they require solving a sequence of strongly coupled problems using, e.g., the fixed point and Newton’s methods [53, 66, 19, 25, 41, 56].

The multi-physics nature of the blood flow problem strongly suggest to employ partitioned (or staggered) numerical algorithms, where the coupled fluid-structure interaction problem is separated into a fluid and a structure sub-problem. The fluid and structure sub-problems are integrated in time in an alternating way, and the coupling conditions are enforced asynchronously. When the density of the structure is much larger than the density of the fluid, as is the case in aeroelasticity, it is sufficient to solve, at every time step, just one fluid sub-problem and one structure sub-problem to obtain a solution. The classical loosely-coupled partitioned schemes of this kind typically use the structure velocity in the fluid sub-problem as Dirichlet data for the fluid velocity (enforcing the no-slip boundary condition at the fluid-structure interface), while in the structure sub-problem the structure is loaded by the fluid normal stress calculated in the fluid sub-problem. These Dirichlet-Neumann loosely-coupled partitioned schemes work well for problems in which the structure is much heavier than the fluid. Unfortunately, when fluid and structure have comparable densities, which is the case in the blood flow application, the simple strategy of separating the fluid from the structure suffers from severe stability issues [16, 57] associated with the added mass effect, discussed in the introduction. The added mass effect reflects itself in Dirichlet-Neumann loosely coupled partitioned schemes by having a poor approximation of the total energy of the coupled problem at every time step of the scheme. A partial solution to this problem is to iterate several times between the fluid and structure sub-solvers at every time step until the energy of the continuous problem is well approximated. These strongly-coupled partitioned schemes, however, are computationally expensive and may suffer from convergence issues for certain parameter values [16].

To get around these difficulties, and to retain the main advantages of loosely-coupled partitioned schemes such as modularity, simple implementation, and low computational costs, several new loosely-coupled algorithms have been proposed recently. In general, they behave quite well for FSI problems containing a thin fluid-structure interface with mass [5, 11, 13, 39, 66, 26, 29, 27, 28, 1, 2, 7, 69, 64, 19, 18].

For FSI problem in which the structure is “thick” relative to the fluid, i.e., the thickness of the structure is comparable to the transverse dimension of the fluid domain, partitioned, loosely-coupled schemes are more difficult to construct. In fact, to the best of our knowledge, there have been no loosely-

coupled, partitioned schemes proposed so far in literature for a class of FSI problems in hemodynamics that contain thick structure models to study the elastodynamics of arterial walls. The closest works in this direction include a strongly-coupled partition scheme by Badia et al. in [6], an explicit scheme by Burman and Fernández where certain “defect-correction” sub-iterations are necessary to achieve optimal accuracy [15], and an operator-splitting scheme by Bukač et al. [14] where a version of Lie splitting was used to design a modular, “semi-partitioned” scheme.

Recently, a novel loosely coupled partitioned scheme, called the Kinematically Coupled  $\beta$ -Scheme, was introduced by Bukač, Čanić et al. in [11, 13], and applied to FSI problems with thin elastic and viscoelastic structures, modeled by the membrane or shell equations. This scheme successfully deals with stability problems associated with the added mass effect in a way different from those reported above. Stability is achieved by combining the structure inertia with the fluid sub-problem to mimic the energy balance of the continuous, coupled problem. It was shown in [74] that the scheme is unconditionally stable even for the parameters associated with the blood flow applications. Additionally, Muha and Čanić showed that a version of this scheme with  $\beta = 0$  converges to a weak solution of the fully nonlinear FSI problem [62]. The case  $\beta = 0$  considered in [62] corresponds to the classical kinematically-coupled scheme, first introduced in [39]. Parameter  $\beta$  was introduced in [11] to increase the accuracy of the scheme. It was shown in [11] that the accuracy of the kinematically-coupled  $\beta$ -scheme with  $\beta = 1$  was comparable to that of monolithic scheme by Badia, Quaini, and Quarteroni in [7] when applied to the nonlinear benchmark FSI problem in hemodynamics, introduced by Formaggia et al. in [32]. A different approach to increasing the accuracy of the classical kinematically-coupled scheme was recently proposed by Fernández et al. [26, 29, 27]. Their modified kinematically-coupled scheme, called “the incremental displacement-correction scheme” treats the structure displacement explicitly in the fluid sub-step and then corrects it in the structure sub-step. Fernández et al. showed that the accuracy of the incremental displacement-correction scheme is first-order in time. The results were obtained for a FSI problem involving a thin elastic structure.

These recent results indicate that the kinematically-coupled scheme and its modifications provide an appealing way to study multi-physics problems involving FSI. Indeed, due to its simple implementation, modularity, and very good performance, modifications of this scheme have been used by several authors to study different multi-physics problems involving FSI, such as FSI between artery, blood flow, and cardiovascular device called stent [61], FSI with poroelastic structures [12], and FSI involving non-Newtonian fluids

[43, 54].

In the present paper we extend this scheme, in combination with the Arbitrary Lagrangian-Eulerian approach, to study fluid structure interaction involving biological composite structures such as arterial walls. Using a combination of analytical and numerical methods new results that reveal novel physical properties of the coupled FSI system are revealed. They include regularizing effects of the fluid-structure interface with mass, and convergence, as the thickness of the thin fluid-structure interface with mass converges to zero, to the FSI solution involving a single thick structure with the thickness equal to the (fixed) combined thickness of the composite structure.

## 2. The splitting algorithm

To numerically solve the fluid-multilayered structure interaction problem (1)-(16) we propose a loosely coupled scheme based on the Lie operator splitting algorithm [34]. The proposed scheme is an extension of the kinematically coupled  $\beta$ -scheme introduced in [11] to study the interaction between an incompressible, viscous fluid and a thin structure modeled by the Koiter shell equations. The scheme was shown to be unconditionally stable and therefore independent of the fluid and structure densities [74]. The unconditional stability is achieved by including the thin structure inertia into the fluid sub-problem as Robin-type boundary condition.

Following similar ideas, the proposed strategy for solving problem (1)-(16) is to split the thin structure equations into the inertia part (plus the viscous part if the structure is viscoelastic), and the remaining elastodynamics part. The inertia part (plus structural viscosity) is then used in the fluid sub-problem as Robin-type boundary condition, while the remaining elastodynamics part is used in the structural sub-problem as a Robin-type boundary condition for the thick structure problem. This strategy ensures unconditional stability of the scheme. To increase the accuracy, the fluid stress will be split so that a portion corresponding to the fluid pressure is used as loading in the structure sub-problem. To further increase the accuracy of the scheme, the fluid sub-problem can be split into a time-dependent Stokes problem (with the Robin-type boundary condition mentioned above) plus the remaining advection sub-problem. This enables the use of conservative schemes to solve the advection sub-problem, if so desired.



### 2.1. The Lie scheme and the first-order system

To apply the Lie splitting scheme the problem must first be written as a first-order system in time:

$$\frac{\partial \phi}{\partial t} + A(\phi) = 0, \quad \text{in } (0, T), \quad (34)$$

$$\phi(0) = \phi_0, \quad (35)$$

where  $A$  is an operator from a Hilbert space into itself. Operator  $A$  is then split, in a non-trivial decomposition, as

$$A = \sum_{i=1}^I A_i. \quad (36)$$

The Lie scheme consists of the following. Let  $\Delta t > 0$  be a time discretization step. Denote  $t^n = n\Delta t$  and let  $\phi^n$  be an approximation of  $\phi(t^n)$ . Set  $\phi^0 = \phi_0$ . Then, for  $n \geq 0$  compute  $\phi^{n+1}$  by solving

$$\frac{\partial \phi_i}{\partial t} + A_i(\phi_i) = 0 \quad \text{in } (t^n, t^{n+1}), \quad (37)$$

$$\phi_i(t^n) = \phi^{n+(i-1)/I}, \quad (38)$$

and then set  $\phi^{n+i/I} = \phi_i(t^{n+1})$ , for  $i = 1, \dots, I$ .

This method is first-order accurate in time. More precisely, if (34) is defined on a finite-dimensional space, and if the operators  $A_i$  are smooth enough, then  $\|\phi(t^n) - \phi^n\| = O(\Delta t)$  [34]. In our case, operator  $A$  that is associated with problem (1)-(16) will be split into a sum of three operators:

**A1.** The thick structure elastodynamics problem with thin structure elastodynamics included as Robin-type boundary condition.

**A2(a).** A time-dependent Stokes problem with thin structure inertia included as Robin boundary condition.

**A2(b).** The fluid advection problem.

Operator A1 defines a structure problem. Operators A2(a) and A2(b) define a fluid problem.

To rewrite system (1)-(16) in first-order form, we introduce two new variables denoting the thin and thick structure velocities:

$$\hat{\xi} = \frac{\partial \hat{\eta}}{\partial t} \quad \text{and} \quad \hat{V} = \frac{\partial \hat{U}}{\partial t}.$$

System (1)-(16) can be written in first-order ALE form as follows: Find  $\mathbf{v} = (v_z, v_r)$ ,  $p$ ,  $\hat{\boldsymbol{\eta}} = (\hat{\eta}_z, \hat{\eta}_r)$ ,  $\hat{\boldsymbol{\xi}} = (\hat{\xi}_z, \hat{\xi}_r)$ ,  $\hat{\mathbf{U}} = (\hat{U}_z, \hat{U}_r)$  and  $\hat{\mathbf{V}} = (\hat{V}_z, \hat{V}_r)$ , with  $\hat{\mathbf{v}}(\hat{\mathbf{x}}, t) = \mathbf{v}(\mathcal{A}_t(\hat{\mathbf{x}}), t)$ , such that

$$\rho_f \left( \frac{\partial \mathbf{v}}{\partial t} \Big|_{\hat{\mathbf{x}}} + (\mathbf{v} - \mathbf{w}) \cdot \nabla \mathbf{v} \right) = \nabla \cdot \boldsymbol{\sigma}^f(\mathbf{v}, p) \quad \text{in } \Omega^f(t) \times (0, T), \quad (39a)$$

$$\nabla \cdot \mathbf{v} = 0 \quad \text{in } \Omega^f(t) \times (0, T), \quad (39b)$$

$$\rho_m h \frac{\partial \hat{\xi}_z}{\partial t} - C_2 \frac{\partial \hat{\eta}_r}{\partial \hat{z}} - C_1 \frac{\partial^2 \hat{\eta}_z}{\partial \hat{z}^2} = \hat{f}_z \quad \text{on } \hat{\Gamma} \times (0, T), \quad (39c)$$

$$\rho_m h \frac{\partial \hat{\xi}_r}{\partial t} + C_0 \hat{\eta}_r + C_2 \frac{\partial \hat{\eta}_z}{\partial \hat{z}} = \hat{f}_r \quad \text{on } \hat{\Gamma} \times (0, T), \quad (39d)$$

$$\frac{\partial \hat{\boldsymbol{\eta}}}{\partial t} = \hat{\boldsymbol{\xi}} \quad \text{on } \hat{\Gamma} \times (0, T), \quad (39e)$$

$$\rho_s \frac{\partial \hat{\mathbf{V}}}{\partial t} + \gamma \hat{\mathbf{U}} = \nabla \cdot \boldsymbol{\sigma}^s(\hat{\mathbf{U}}) \quad \text{in } \hat{\Omega}^s \times (0, T), \quad (39f)$$

$$\frac{\partial \hat{\mathbf{U}}}{\partial t} = \hat{\mathbf{V}} \quad \text{in } \hat{\Omega}^s \times (0, T), \quad (39g)$$

with the following coupling conditions at the fluid-structure interface:

$$\boldsymbol{\xi} = \mathbf{v}|_{\Gamma(t)}, \quad \hat{\boldsymbol{\eta}} = \hat{\mathbf{U}}|_{\hat{\Gamma}}, \quad (40)$$

$$\rho_m h \frac{\partial (\widehat{v_z|_{\Gamma(t)}})}{\partial t} - C_2 \frac{\partial \hat{\eta}_r}{\partial \hat{z}} - C_1 \frac{\partial^2 \hat{\eta}_z}{\partial \hat{z}^2} + J \widehat{\boldsymbol{\sigma}^f \mathbf{n}^f}|_{\Gamma(t)} \cdot \mathbf{e}_z + \boldsymbol{\sigma}^s \mathbf{n}^s|_{\hat{\Gamma}} \cdot \mathbf{e}_z = 0, \quad (41)$$

$$\rho_m h \frac{\partial (\widehat{v_r|_{\Gamma(t)}})}{\partial t} + C_0 \hat{\eta}_r + C_2 \frac{\partial \hat{\eta}_z}{\partial \hat{z}} + J \widehat{\boldsymbol{\sigma}^f \mathbf{n}^f}|_{\Gamma(t)} \cdot \mathbf{e}_r + \boldsymbol{\sigma}^s \mathbf{n}^s|_{\hat{\Gamma}} \cdot \mathbf{e}_r = 0. \quad (42)$$

This problem is supplemented with the boundary and initial conditions presented in Section 1.2.

## 2.2. Details of the operator-splitting scheme

The following splitting of the fluid stress  $\widehat{\boldsymbol{\sigma}^f \mathbf{n}^f}$  will be used in the splitting algorithm:

$$\widehat{\boldsymbol{\sigma}^f \mathbf{n}^f} = \underbrace{\widehat{\boldsymbol{\sigma}^f \mathbf{n}^f} + \beta \widehat{p \mathbf{n}^f}}_{(Part \ I)} - \underbrace{\beta \widehat{p \mathbf{n}^f}}_{(Part \ II)},$$

where  $\beta \in [0, 1]$ . Part I of the fluid stress will be included in the Robin-type boundary condition for the fluid sub-problem, while Part II of the fluid stress will be included in the Robin-type boundary condition for the thick structure equations. Details of the scheme are as follows.

**Problem A1:** This problem involves solving the thick structure problem on  $\hat{\Omega}_S$ , with membrane elastodynamics serving as Robin-type boundary condition on  $\hat{\Gamma}$ . The Robin boundary condition also includes Part II of the normal fluid stress, evaluated at the previous time-step, as part of the loading for the elastodynamics of the thin structure. After computing the thin and thick structure displacement, the domain velocity is computed and used in the fluid sub-problem in ALE mapping. The trace of the fluid velocity from the previous time step serves as initial data for the structure velocity in this problem. Thus, the structure “feels” the fluid via the initial data and Part II of the normal fluid stress.

To be consistent with the notation in the Lie splitting scheme, we write Problem A1 in first-order form, i.e., as a first-order system in time, including all the variables in the problem. However, by using the kinematic coupling condition, one can simplify the expression for the boundary condition on  $\hat{\Gamma}$ , as presented in Remark 1 below, in which case the present problem becomes a pure structure problem, driven by the fluid velocity initial data and fluid normal stress.

The problem reads: Find  $\mathbf{v}, \hat{\boldsymbol{\eta}}, \hat{\boldsymbol{\xi}}, \hat{\mathbf{V}}$ , and  $\hat{\mathbf{U}}$ , with  $\hat{\mathbf{v}}(\hat{\mathbf{x}}, t) = \mathbf{v}(\mathcal{A}_t(\hat{\mathbf{x}}), t)$  such that:

$$\left. \begin{aligned} \rho_s \frac{\partial \hat{\mathbf{V}}}{\partial t} + \gamma \hat{\mathbf{U}} &= \nabla \cdot \boldsymbol{\sigma}^s(\hat{\mathbf{U}}) \\ \frac{\partial \hat{\mathbf{U}}}{\partial t} &= \hat{\mathbf{V}} \end{aligned} \right\} \text{ in } \hat{\Omega}^s \times (t^n, t^{n+1}), \quad (43)$$

satisfying the following conditions on  $\hat{\Gamma} \times (t^n, t^{n+1})$ :

$$\begin{aligned} \rho_m h \frac{\partial(\widehat{v_z|_{\Gamma(t)}})}{\partial t} - C_2 \frac{\partial \hat{\eta}_r}{\partial \hat{z}} - C_1 \frac{\partial^2 \hat{\eta}_z}{\partial \hat{z}^2} + \boldsymbol{\sigma}^s \mathbf{n}^s|_{\hat{\Gamma}} \cdot \mathbf{e}_z &= J^n \beta p^n \widehat{\mathbf{n}^f|_{\Gamma(t)}} \cdot \mathbf{e}_z, \\ \rho_m h \frac{\partial(\widehat{v_r|_{\Gamma(t)}})}{\partial t} + C_0 \hat{\eta}_r + C_2 \frac{\partial \hat{\eta}_z}{\partial \hat{z}} + \boldsymbol{\sigma}^s \mathbf{n}^s|_{\hat{\Gamma}} \cdot \mathbf{e}_r &= J^n \beta p^n \widehat{\mathbf{n}^f|_{\Gamma(t)}} \cdot \mathbf{e}_r, \\ \frac{\partial \hat{\boldsymbol{\eta}}}{\partial t} &= \hat{\boldsymbol{\xi}}, \quad \boldsymbol{\xi} = \mathbf{v}|_{\Gamma(t)}, \quad \hat{\boldsymbol{\eta}} = \hat{\mathbf{U}}|_{\hat{\Gamma}}, \end{aligned}$$

and satisfying the following boundary conditions at  $z = 0, L$  and at  $\hat{\Gamma}_{ext}^s$ :

$$\begin{aligned} \hat{\mathbf{U}}|_{z=0, L} &= 0, \\ \hat{\mathbf{U}}_z &= 0, \quad \mathbf{n}_{ext}^s \cdot \boldsymbol{\sigma}^s \mathbf{n}_{ext}^s = 0 \quad \text{on } \hat{\Gamma}_{ext}^s \times (t^n, t^{n+1}). \end{aligned}$$

The initial conditions are given by the values of the unknown functions at the end of the previous time step:

$$\mathbf{v}(t^n) = \mathbf{v}^n, \hat{\boldsymbol{\eta}}(t^n) = \hat{\boldsymbol{\eta}}^n, \hat{\boldsymbol{\xi}}(t^n) = \hat{\boldsymbol{\xi}}^n, \hat{\mathbf{U}}(t^n) = \hat{\mathbf{U}}^n, \hat{\mathbf{V}}(t^n) = \hat{\mathbf{V}}^n.$$

The fluid velocity remains unchanged:

$$\left. \frac{\partial \mathbf{v}}{\partial t} \right|_{\hat{\mathbf{x}}} = 0 \text{ in } \Omega^f(t^n) \times (t^n, t^{n+1}).$$

The values of the just calculated variables are set to be  $\mathbf{v}^{n+1/3} = \mathbf{v}(t^{n+1})$ ,  $\hat{\boldsymbol{\eta}}^{n+1/3} = \hat{\boldsymbol{\eta}}(t^{n+1})$ ,  $\hat{\boldsymbol{\xi}}^{n+1/3} = \hat{\boldsymbol{\xi}}(t^{n+1})$ ,  $\hat{\mathbf{U}}^{n+1/3} = \hat{\mathbf{U}}(t^{n+1})$ ,  $\hat{\mathbf{V}}^{n+1/3} = \hat{\mathbf{V}}(t^{n+1})$ ,  $p^{n+1} = p(t^{n+1})$ .

Using the just-calculated values of the thin structure displacement and velocity we compute the ALE velocity  $\mathbf{w}$  by defining  $\mathcal{A}_{t^{n+1}}$  to be the harmonic extension of the structure displacement  $\hat{\boldsymbol{\eta}}^{n+1/3}$  at the fluid-structure interface onto the whole domain  $\hat{\Omega}^f$

$$\begin{aligned} \Delta \mathcal{A}_{t^{n+1}} &= 0 \text{ in } \hat{\Omega}^f, \\ \mathcal{A}_{t^{n+1}}|_{\hat{\Gamma}} &= \hat{\boldsymbol{\eta}}^{n+1/3}, \\ \mathcal{A}_{t^{n+1}}|_{\partial\hat{\Omega}^f \setminus \hat{\Gamma}} &= 0. \end{aligned}$$

Then, we define  $\mathbf{w}^{n+1} = \frac{\partial \mathcal{A}_{t^{n+1}}}{\partial t} = \frac{\partial \mathbf{x}}{\partial t} \approx \frac{\mathbf{x}^{n+1} - \mathbf{x}^n}{\Delta t}$ , which remains unchanged in Problems 2(a) and 2(b).

**Remark 1.** Note that using the kinematic coupling conditions, we can rewrite the membrane equations in the following way:

$$\begin{aligned} \rho_m h \frac{\partial \hat{V}_z}{\partial t} - C_2 \frac{\partial \hat{U}_r}{\partial \hat{z}} - C_1 \frac{\partial^2 \hat{U}_z}{\partial \hat{z}^2} + \boldsymbol{\sigma}^s \mathbf{n}^s|_{\hat{\Gamma}} \cdot \mathbf{e}_z &= J^n \beta p^n \widehat{\mathbf{n}^f|_{\Gamma(t)}} \cdot \mathbf{e}_z, \text{ on } \hat{\Gamma} \times (t^n, t^{n+1}), \\ \rho_m h \frac{\partial \hat{V}_r}{\partial t} + C_0 \hat{U}_r + C_2 \frac{\partial \hat{U}_z}{\partial \hat{z}} + \boldsymbol{\sigma}^s \mathbf{n}^s|_{\hat{\Gamma}} \cdot \mathbf{e}_r &= J^n \beta p^n \widehat{\mathbf{n}^f|_{\Gamma(t)}} \cdot \mathbf{e}_r \text{ on } \hat{\Gamma} \times (t^n, t^{n+1}). \end{aligned}$$

In this way the membrane equations become a Robin-type boundary condition for the thick structure problem, and Problem A1 becomes a pure structure problem.

**Problem A2(a).** This problem involves solving a time dependent Stokes problem with Robin-type boundary conditions involving the structure inertia and Part I of the fluid stress. This problem is solved on a fixed fluid domain  $\Omega^f(t^n)$ , which is determined by the location of the structure position calculated in the previous time step. To increase the accuracy, one

can also use the just-updated structure position and solve the fluid sub-problem on domain  $\Omega^f(t^{n+1})$ . In the proof of stability of this scheme, the use of  $\Omega^f(t^n)$  is more convenient.

Similarly as before, we formally write the problem in terms of all the unknowns in the coupled problem. However, after a close inspection of the problem, one can see that this is a pure fluid sub-problem, which communicates with the structure problem via the thin structure inertia in the Robin-type boundary condition on  $\hat{\Gamma}$ , the updated fluid domain obtained from the structure problem in the previous time-step, and via the initial data for the trace of the fluid velocity on  $\hat{\Gamma}$ , given by the velocity of the thin structure, obtained from the just calculated structure step.

The problem reads as follows: Find  $\mathbf{v}, p, \hat{\boldsymbol{\eta}}, \hat{\boldsymbol{\xi}}, \hat{\mathbf{V}}$  and  $\hat{\mathbf{U}}$ , with  $\hat{\mathbf{v}}(\hat{\mathbf{x}}, t) = \mathbf{v}(\mathcal{A}_t(\hat{\mathbf{x}}), t)$  such that for  $t \in (t^n, t^{n+1})$ , with  $p^n$  obtained at the previous time step, the following holds:

$$\left. \begin{aligned} \rho_f \frac{\partial \mathbf{v}}{\partial t} \Big|_{\hat{\mathbf{x}}} &= \nabla \cdot \boldsymbol{\sigma}^f \\ \nabla \cdot \mathbf{v} &= 0 \end{aligned} \right\} \text{ in } \Omega^f(t^n) \times (t^n, t^{n+1}), \quad (44)$$

with the Robin-type boundary condition on  $\hat{\Gamma} \times (t^n, t^{n+1})$  given by:

$$\rho_m h \frac{\partial(\widehat{\mathbf{v}}|_{\Gamma(t)})}{\partial t} + J(\widehat{\boldsymbol{\sigma}^f \mathbf{n}^f}|_{\Gamma(t)} + \beta p^n \widehat{\mathbf{n}^f}|_{\Gamma(t)}) = 0.$$

This is supplemented with the following inlet and outlet boundary conditions on  $(t^n, t^{n+1})$ :

$$\mathbf{v}(0, R, t) = \mathbf{v}(L, R, t) = 0,$$

$$\boldsymbol{\sigma}^f \mathbf{n}_{in}^f = -p_{in}(t) \mathbf{n}_{in}^f \text{ on } \Gamma_{in}^f, \quad \boldsymbol{\sigma}^f \mathbf{n}_{out}^f = -p_{out}(t) \mathbf{n}_{out}^f \text{ on } \Gamma_{out}^f,$$

and the following symmetry boundary conditions at  $r = 0$ :

$$\frac{\partial v_z}{\partial r}(z, 0, t) = v_r(z, 0, t) = 0 \quad \text{on } (0, L) \times (t^n, t^{n+1}).$$

The location of the structure remains unchanged:

$$\begin{aligned} \frac{\partial \hat{\boldsymbol{\eta}}}{\partial t} &= 0 & \text{on } \hat{\Gamma} \times (t^n, t^{n+1}), \\ \frac{\partial \hat{\mathbf{V}}}{\partial t} = \frac{\partial \hat{\mathbf{U}}}{\partial t} &= 0 & \text{in } \hat{\Omega}^s \times (t^n, t^{n+1}). \end{aligned}$$

The initial conditions are given by:

$$\mathbf{v}(t^n) = \mathbf{v}^{n+1/3}, \quad \hat{\boldsymbol{\eta}}(t^n) = \hat{\boldsymbol{\eta}}^{n+1/3}, \quad \hat{\boldsymbol{\xi}}(t^n) = \hat{\boldsymbol{\xi}}^{n+1/3}, \quad \hat{\mathbf{U}}(t^n) = \hat{\mathbf{U}}^{n+1/3}, \quad \text{and} \\ \hat{\mathbf{V}}(t^n) = \hat{\mathbf{V}}^{n+1/3}.$$

After a solution to this problem is calculated, set  $\mathbf{v}^{n+2/3} = \mathbf{v}(t^{n+1})$ ,  $\hat{\boldsymbol{\eta}}^{n+2/3} = \hat{\boldsymbol{\eta}}(t^{n+1})$ ,  $\hat{\boldsymbol{\xi}}^{n+2/3} = \hat{\boldsymbol{\xi}}(t^{n+1})$ ,  $\hat{\mathbf{U}}^{n+2/3} = \hat{\mathbf{U}}(t^{n+1})$ ,  $\hat{\mathbf{V}}^{n+2/3} = \hat{\mathbf{V}}(t^{n+1})$ ,  $p^{n+1} = p(t^{n+1})$ .

**Problem A2(b).** Solve the fluid and ALE advection sub-problem defined on the fixed domain  $\Omega^f(t^n)$ , with the domain velocity  $\mathbf{w}^{n+1}$  just calculated in Problem A1.

The problem reads: Find  $\mathbf{v}, \hat{\boldsymbol{\eta}}, \hat{\boldsymbol{\xi}}, \hat{\mathbf{V}}$  and  $\hat{\mathbf{U}}$ , with  $\hat{\mathbf{v}}(\hat{\mathbf{x}}, t) = \mathbf{v}(\mathcal{A}_t(\hat{\mathbf{x}}), t)$  and  $\mathbf{w}^{n+1}$  computed in Problem A1, such that:

$$\left. \frac{\partial \mathbf{v}}{\partial t} \right|_{\hat{\mathbf{x}}} + (\mathbf{v}^n - \mathbf{w}^{n+1}) \cdot \nabla \mathbf{v} = 0 \quad \text{in } \Omega^f(t^n) \times (t^n, t^{n+1}),$$

with the lateral boundary condition on  $\hat{\Gamma} \times (t^n, t^{n+1})$  given by

$$\rho_m h \frac{\partial(\widehat{\mathbf{v}|_{\Gamma(t)}})}{\partial t} = 0,$$

and with the inlet/outlet boundary conditions defined on the portion of the boundary for which the slope of the characteristics associated with the advection problem, defined by the sign of  $(\mathbf{v}^n - \mathbf{w}^{n+1}) \cdot \mathbf{n}$ , is pointing inward, toward the fluid domain :

$$\mathbf{v} = \mathbf{v}^{n+2/3}, \quad \text{on } \Gamma_-^{n+2/3}, \quad \text{where}$$

$$\Gamma_-^{n+2/3} = \{\mathbf{x} \in \mathbb{R}^2 | \mathbf{x} \in \partial\Omega^f(t^n), (\mathbf{v}^n - \mathbf{w}^{n+1}) \cdot \mathbf{n} < 0\}.$$

The structure does not change in this step:

$$\begin{aligned} \frac{\partial \hat{\boldsymbol{\eta}}}{\partial t} &= 0 & \text{on } \hat{\Gamma} \times (t^n, t^{n+1}), \\ \frac{\partial \hat{\mathbf{V}}}{\partial t} &= \frac{\partial \hat{\mathbf{U}}}{\partial t} = 0 & \text{in } \hat{\Omega}^s \times (t^n, t^{n+1}), \end{aligned}$$

The initial conditions are given by the solution obtained in Problem A2(a):

$$\mathbf{v}(t^n) = \mathbf{v}^{n+2/3}, \quad \hat{\boldsymbol{\eta}}(t^n) = \hat{\boldsymbol{\eta}}^{n+2/3}, \quad \hat{\boldsymbol{\xi}}(t^n) = \hat{\boldsymbol{\xi}}^{n+2/3}, \quad \hat{\mathbf{U}}(t^n) = \hat{\mathbf{U}}^{n+2/3}, \quad \text{and} \\ \hat{\mathbf{V}}(t^n) = \hat{\mathbf{V}}^{n+2/3}.$$

Then set  $\mathbf{v}^{n+1} = \mathbf{v}(t^{n+1})$ ,  $\hat{\boldsymbol{\eta}}^{n+1} = \hat{\boldsymbol{\eta}}(t^{n+1})$ ,  $\hat{\boldsymbol{\xi}}^{n+1} = \hat{\boldsymbol{\xi}}(t^{n+1})$ ,  $\hat{\mathbf{U}}^{n+1} = \hat{\mathbf{U}}(t^{n+1})$ ,  $\hat{\mathbf{V}}^{n+1} = \hat{\mathbf{V}}(t^{n+1})$ .

After this step we update the fluid domain position via

$$\Omega^f(t^{n+1}) = \mathcal{A}_{t^{n+1}}(\hat{\Omega}^f).$$

Then set  $t^n = t^{n+1}$  and return to Problem A1.

### 3. Discretized scheme in weak form

As mentioned above, discretization in time is obtained by subdividing the time interval  $(0, T)$  into  $N$  sub-intervals of width  $\Delta t$ , and denoting  $t^n = n\Delta t$ , where  $n \leq N$ . The Backward Euler scheme is used to approximate the time derivatives on each  $(t^{n+1}, t^n)$ . For the space discretization, we use the finite element method approach, based on a conforming FEM triangulation with maximum triangle diameter  $k$ . For this purpose, we define the finite element spaces  $V_k^f(t^n) \subset V^f(t^n)$ ,  $Q_k(t^n) \subset Q(t^n)$ ,  $\hat{V}_k^m \subset \hat{V}^m$  and  $\hat{V}_k^s \subset \hat{V}^s$ , and introduce the following bilinear forms

$$\begin{aligned}
a_f^n(\mathbf{v}, \boldsymbol{\varphi}) &:= 2\mu_f \int_{\Omega^f(t^n)} \mathbf{D}(\mathbf{v}) : \mathbf{D}(\boldsymbol{\varphi}) d\mathbf{x}, \\
b_f^n(p, \boldsymbol{\varphi}) &:= \int_{\Omega^f(t^n)} p \nabla \cdot \boldsymbol{\varphi} d\mathbf{x}, \\
\hat{a}_m(\hat{\boldsymbol{\eta}}, \hat{\boldsymbol{\zeta}}) &:= C_1 \int_0^L \frac{\partial \hat{\eta}_z}{\partial \hat{z}} \frac{\partial \hat{\zeta}_z}{\partial \hat{z}} d\hat{z} + C_0 \int_0^L \hat{\eta}_r \hat{\zeta}_r d\hat{z} \\
&\quad + C_2 \int_0^L \frac{\partial \hat{\eta}_z}{\partial \hat{z}} \hat{\zeta}_r d\hat{z} - C_2 \int_0^L \frac{\partial \hat{\eta}_r}{\partial \hat{z}} \hat{\zeta}_z d\hat{z}, \\
\hat{a}_e(\hat{\mathbf{U}}, \hat{\boldsymbol{\psi}}) &:= 2\mu_s \int_{\hat{\Omega}^s} \mathbf{D}(\hat{\mathbf{U}}) : \mathbf{D}(\hat{\boldsymbol{\psi}}) d\hat{\mathbf{x}} + \lambda_s \int_{\hat{\Omega}^s} (\nabla \cdot \hat{\mathbf{U}})(\nabla \cdot \hat{\boldsymbol{\psi}}) d\hat{\mathbf{x}} \\
&\quad + \gamma \int_{\hat{\Omega}^s} \hat{\mathbf{U}} \cdot \hat{\boldsymbol{\psi}} d\hat{\mathbf{x}}.
\end{aligned}$$

Discretization of the operator splitting scheme discussed above, in weak form, is given by the following:

**Problem A1. (The structure problem)** To discretize the structure problem in time we use the second order Newmark scheme. The problem reads as follows: Find  $(\hat{\mathbf{U}}_k^{n+1/3}, \hat{\mathbf{V}}_k^{n+1/3}) \in \hat{V}_h^s \times \hat{V}_k^s$  such that for all  $(\hat{\boldsymbol{\psi}}_k, \hat{\boldsymbol{\phi}}_k) \in \hat{V}_k^s \times \hat{V}_k^s$

$$\begin{aligned}
&\rho_s \int_{\hat{\Omega}^s} \frac{\hat{\mathbf{V}}_k^{n+1/3} - \hat{\mathbf{V}}_k^n}{\Delta t} \cdot \hat{\boldsymbol{\psi}}_k d\hat{\mathbf{x}} + \gamma \int_{\hat{\Omega}^s} \frac{\hat{\mathbf{U}}_k^n + \hat{\mathbf{U}}_k^{n+1/3}}{2} \cdot \hat{\boldsymbol{\psi}}_k d\hat{\mathbf{x}} \\
&\quad + \rho_m h \int_0^L \frac{\hat{\mathbf{V}}_k^{n+1/3} - \hat{\mathbf{V}}_k^n}{\Delta t} \cdot \hat{\boldsymbol{\psi}}_k d\hat{z} + \hat{a}_m\left(\frac{\hat{\mathbf{U}}_k^n + \hat{\mathbf{U}}_k^{n+1/3}}{2}, \hat{\boldsymbol{\psi}}_k\right) \\
&\quad + \hat{a}_e\left(\frac{\hat{\mathbf{U}}_k^n + \hat{\mathbf{U}}_k^{n+1/3}}{2}, \hat{\boldsymbol{\psi}}_k\right) + \rho_s \int_{\hat{\Omega}^s} \left(\frac{\hat{\mathbf{V}}_k^n + \hat{\mathbf{V}}_k^{n+1/3}}{2} - \frac{\hat{\mathbf{U}}_k^{n+1/3} - \hat{\mathbf{U}}_k^n}{\Delta t}\right) \cdot \hat{\boldsymbol{\phi}}_k d\hat{\mathbf{x}}
\end{aligned}$$

$$\begin{aligned}
& +\rho_m h \int_0^L \left( \frac{\hat{\mathbf{V}}_k^n + \hat{\mathbf{V}}_k^{n+1/3}}{2} - \frac{\hat{\mathbf{U}}_k^{n+1/3} - \hat{\mathbf{U}}_k^n}{\Delta t} \right) \cdot \hat{\boldsymbol{\phi}}_k d\hat{z} \\
& = \int_0^L J^n \beta p^n \widehat{\mathbf{n}^f}|_{\Gamma(t)} \cdot \hat{\boldsymbol{\psi}}_k d\hat{z}.
\end{aligned} \tag{45}$$

Note that in this step we take all the kinematic coupling conditions into account: initially we set  $\hat{\mathbf{V}}_k^n|_{\Gamma} = \hat{\boldsymbol{\xi}}_k^n = \widehat{\mathbf{v}_k^n|_{\Gamma(t^n)}}$ ; then, once  $\hat{\mathbf{U}}_k^{n+1/3}$  and  $\hat{\mathbf{V}}_k^{n+1/3}$  are computed,  $\hat{\boldsymbol{\eta}}_k^{n+1/3}$ ,  $\hat{\boldsymbol{\xi}}_k^{n+1/3}$  and  $\widehat{\mathbf{v}_k^{n+1/3}|_{\Gamma(t^n)}}$  can be recovered via  $\hat{\boldsymbol{\eta}}_k^{n+1/3} = \hat{\mathbf{U}}_k^{n+1/3}|_{\Gamma}$  and  $\hat{\boldsymbol{\xi}}_k^{n+1/3} = \widehat{\mathbf{v}_k^{n+1/3}|_{\Gamma(t^n)}} = \hat{\mathbf{V}}_k^{n+1/3}|_{\Gamma}$ .

In this step  $\partial \mathbf{v}_k / \partial t = 0$ , and so  $\mathbf{v}_k^{n+1/3} = \mathbf{v}_k^n$ .

At the end of this step we compute the new fluid domain velocity by finding  $\mathcal{A}_{t^{n+1}} \in (H^1(\hat{\Omega}^f))^2$  with  $\mathcal{A}_{t^{n+1}}|_{\hat{\Gamma}} = \hat{\boldsymbol{\eta}}^{n+1/3}$  and  $\mathcal{A}_{t^{n+1}}|_{\partial\hat{\Omega}^f \setminus \hat{\Gamma}} = 0$ , such that

$$\int_{\hat{\Omega}^f} \nabla \mathcal{A}_{t^{n+1}} \cdot \nabla \zeta d\hat{\mathbf{x}} = 0, \quad \forall \zeta \in (H_0^1(\hat{\Omega}^f))^2. \tag{46}$$

Then, the new fluid domain velocity is given by

$$\mathbf{w}^{n+1} = \frac{\partial \mathcal{A}_{t^{n+1}}}{\partial t} \approx \frac{\mathcal{A}_{t^{n+1}}(\hat{\mathbf{x}}) - \mathbf{x}^n}{\Delta t}.$$

**Problem A2(a). (The time dependent Stokes problem)** We discretize Problem A2(a) using the Backward Euler scheme, giving rise to the following weak formulation: Find  $(\mathbf{v}_k^{n+2/3}, p_k^{n+1}) \in V_k^f(t^n) \times Q_k(t^n)$  such that for all  $(\boldsymbol{\varphi}_k, q_k) \in V_k^f(t^n) \times Q_k(t^n)$

$$\begin{aligned}
& \rho_f \int_{\Omega^f(t^n)} \frac{\mathbf{v}_k^{n+2/3} - \mathbf{v}_k^{n+1/3}}{\Delta t} \cdot \boldsymbol{\varphi}_k d\mathbf{x} + a_f^n(\mathbf{v}_k^{n+2/3}, \boldsymbol{\varphi}_k) - b_f^n(p_k^{n+1}, \boldsymbol{\varphi}_k) \\
& + b_f^n(q_k, \mathbf{v}_k^{n+2/3}) + \rho_m h \int_0^L \frac{\widehat{\mathbf{v}_k^{n+2/3}|_{\Gamma(t^n)}} - \widehat{\mathbf{v}_k^{n+1/3}|_{\Gamma(t^n)}}}{\Delta t} \cdot \hat{\boldsymbol{\varphi}}_k d\hat{x} \\
& = \int_0^R p_{in}(t^{n+1}) \varphi_{z,k}|_{z=0} dr - \int_0^R p_{out}(t^{n+1}) \varphi_{z,k}|_{z=L} dr \\
& \quad - \int_0^L J^n \beta p^n \widehat{\mathbf{n}^f}|_{\Gamma(t)} \cdot \hat{\boldsymbol{\varphi}}_k d\hat{x}.
\end{aligned} \tag{47}$$

In this step the structure is not moving, and so  $\hat{\mathbf{U}}_k^{n+2/3} = \hat{\mathbf{U}}_k^{n+1/3}$ ,  $\hat{\mathbf{V}}_k^{n+2/3} = \hat{\mathbf{V}}_k^{n+1/3}$ ,  $\hat{\boldsymbol{\eta}}_k^{n+2/3} = \hat{\boldsymbol{\eta}}_k^{n+1/3}$ , and  $\hat{\boldsymbol{\xi}}_k^{n+2/3} = \hat{\boldsymbol{\xi}}_k^{n+1/3}$ .



**Problem A2(b). (The fluid and ALE advection)** As in the previous step, we discretize Problem A2(b) using the Backward Euler scheme. The weak formulation reads as follows: Find  $\mathbf{v}_k^{n+1} \in V_k^f(t^n)$  with  $\mathbf{v}_k^{n+1} = \mathbf{v}_k^{n+2/3}$  on  $\Gamma_-^{n+2/3}$ , such that for all  $\boldsymbol{\varphi}_k \in \{\boldsymbol{\varphi}_k \in V_k^f(t^n) \mid \boldsymbol{\varphi}_k = 0 \text{ on } \Gamma_-^{n+2/3}\}$

$$\rho_f \int_{\Omega^f(t^n)} \frac{\mathbf{v}_k^{n+1} - \mathbf{v}_k^{n+2/3}}{\Delta t} \cdot \boldsymbol{\varphi}_k d\mathbf{x} + \rho_f \int_{\Omega^f(t^n)} ((\mathbf{v}_k^n - \mathbf{w}_k^{n+1}) \cdot \nabla) \mathbf{v}_k^{n+1} \cdot \boldsymbol{\varphi}_k = 0. \quad (48)$$

Note that here we use  $\mathbf{w}_k^{n+1}$  computed at the very end of Problem A1.

In this step the structure is not moving, and so

$$\hat{\mathbf{U}}_k^{n+1} = \hat{\mathbf{U}}_k^{n+2/3}, \hat{\mathbf{V}}_k^{n+1} = \hat{\mathbf{V}}_k^{n+2/3}, \hat{\boldsymbol{\eta}}_k^{n+1} = \hat{\boldsymbol{\eta}}_k^{n+2/3}, \hat{\boldsymbol{\xi}}_k^{n+1} = \hat{\boldsymbol{\xi}}_k^{n+2/3}.$$

Finally, we update the fluid domain position via

$$\Omega^f(t^{n+1}) = (\mathbf{I} + \mathcal{A}_{t^{n+1}})(\hat{\Omega}^f).$$

Then, set  $t^n = t^{n+1}$  and return to Problem A1.

#### 4. Unconditional stability of the scheme for $\beta = 0$

We show an energy estimate that is associated with unconditional stability for the scheme when  $\beta = 0$ . We show that the sum of the total energy of the coupled problem plus viscous dissipation of the coupled discretized problem is bounded by the discrete energy of initial data and the work done by the inlet and outlet dynamic pressure data. In contrast with similar results appearing in literature which consider simplified models without fluid advection, and/or linearized fluid-structure coupling calculated at a fixed fluid domain boundary [16, 74, 5, 27, 15], in this manuscript we prove the desired energy estimate for the full, nonlinear FSI problem, that includes fluid advection and nonlinear coupling at the moving fluid-structure interface.

To simplify analysis, the following assumptions that do not influence stability of the scheme will be considered:

1. Only radial displacement of the fluid-structure interface is allowed, i.e.,  $\eta_z = U_z|_{\hat{\Gamma}} = 0$ . In that case, we consider the following equation for the radial membrane displacement

$$\rho_m h \frac{\partial^2 \hat{\eta}_r}{\partial t^2} + C_0 \hat{\eta}_r = \hat{f}_r.$$

The FSI problem with this boundary condition is well-defined.

- 2.** The problem is driven by the dynamic inlet and outlet pressure data, and the flow enters and leaves the fluid domain parallel to the horizontal axis:

$$p + \frac{\rho_f}{2}|\mathbf{v}|^2 = p_{in/out}(t), \quad v_r = 0, \quad \text{on } \Gamma_{in/out}^f.$$

These assumptions do not influence stability issues related to the added mass effect associated with partitioned schemes in FSI in blood flow.

To simplify matters, instead of splitting the Navier-Stokes equations into the time dependent Stokes problem and the advection problem, we keep the fluid problem uncoupled in the stability analysis. Therefore, our splitting scheme becomes:

- A1.** The thick structure problem with membrane elastodynamics as Robin-type boundary condition.
- A2.** The fluid problem modeled by the Navier-Stokes equations in ALE form, with structure inertia included as Robin boundary condition for the fluid problem.

We consider the case  $\beta = 0$  here. Numerical results presented in [11] indicate that only accuracy is affected by changing the parameter  $\beta$  between 0 and 1, and not stability. We mention a related work in [74] where unconditional stability of the kinematically-coupled  $\beta$ -scheme for  $\beta \in [0, 1]$  was proved for a simplified, linearized FSI problem with a thin structure, using different techniques from those presented here.

#### *4.1. Discretized scheme in weak form assuming only radial displacement of the fluid-structure interface*

There are only a few differences with the discretized scheme presented above. The bilinear form  $\hat{a}_m$  associated with the thin structure problem is now simpler and is given by:

$$\hat{a}_m(\hat{\eta}_r, \hat{\zeta}_r) = C_0 \int_0^L \hat{\eta}_r \hat{\zeta}_r d\hat{z}.$$

Furthermore, we consider the problem with  $\beta = 0$ , and the splitting into two sub-problems: the structure and the fluid sub-problem, where, unlike before, the fluid dissipation and advection are treated together in the same step. Finally, since we can easily explicitly calculate an ALE mapping in this case, the calculations of the ALE mapping, ALE velocity and the Jacobian of the ALE mapping are presented explicitly at the end of this sub-section.

They are used in the derivation of the energy estimate, presented in the next sub-section.

For completeness, we present the two steps of the discretized scheme next.

**Problem A1 (Structure).** Find  $(\hat{U}_k^{n+1/2}, \hat{V}_k^{n+1/2}) \in \hat{V}_k^s \times \hat{V}_k^s$  such that for all  $(\hat{\psi}_k, \hat{\phi}_k) \in \hat{V}_k^s \times \hat{V}_k^s$

$$\begin{aligned} & \rho_s \int_{\hat{\Omega}^s} \frac{\hat{V}_k^{n+1/2} - \hat{V}_k^n}{\Delta t} \cdot \hat{\psi}_k d\hat{x} + \gamma \int_{\hat{\Omega}^s} \frac{\hat{U}_k^n + \hat{U}_k^{n+1/2}}{2} \cdot \hat{\psi}_k d\hat{x} \\ & + \rho_m h \int_{\Gamma} \frac{\hat{V}_{r,k}^{n+1/2} - \hat{V}_{r,k}^n}{\Delta t} \hat{\psi}_{r,k} + \hat{a}_m \left( \frac{\hat{U}_{r,k}^n + \hat{U}_{r,k}^{n+1/2}}{2}, \hat{\psi}_{r,k} \right) + \hat{a}_e \left( \frac{\hat{U}_k^n + \hat{U}_k^{n+1/2}}{2}, \hat{\psi}_k \right) \\ & + \rho_s \int_{\hat{\Omega}^s} \left( \frac{\hat{V}_k^n + \hat{V}_k^{n+1/2}}{2} - \frac{\hat{U}_k^{n+1/2} - \hat{U}_k^n}{\Delta t} \right) \cdot \hat{\phi}_k d\hat{x} \\ & + \rho_m h \int_{\Gamma} \left( \frac{\hat{V}_{r,k}^n + \hat{V}_{r,k}^{n+1/2}}{2} - \frac{\hat{U}_{r,k}^{n+1/2} - \hat{U}_{r,k}^n}{\Delta t} \right) \cdot \hat{\phi}_{r,k} d\hat{z} = 0, \end{aligned} \quad (49)$$

with the initial data such that  $\hat{V}_{r,k}^n|_{\Gamma} = \hat{\xi}_{r,k}^n = \widehat{v_{r,k}^n|_{\Gamma(t^n)}}$ .

Then set  $\hat{\eta}_{r,k}^{n+1/2} = \hat{U}_{r,k}^{n+1/2}|_{\Gamma}$  and  $\hat{\xi}_{r,k}^{n+1/2} = \widehat{v_{r,k}^{n+1/2}|_{\Gamma(t^n)}} = \hat{V}_{r,k}^{n+1/2}|_{\Gamma}$ , and, since the fluid velocity does not change,  $\mathbf{v}_k^{n+1/2} = \mathbf{v}_k^n$ .

**Problem A2 (Fluid).** Find  $(\mathbf{v}_k^{n+1}, p_k^{n+1}) \in V_k^f(t^n) \times Q_k(t^n)$  such that for all  $(\varphi_k, q_k) \in V_k^f(t^{n+1}) \times Q_k(t^{n+1})$ :

$$\begin{aligned} & \rho_f \int_{\Omega^f(t^n)} \frac{\mathbf{v}_k^{n+1} - \mathbf{v}_k^{n+1/2}}{\Delta t} \cdot \varphi_k d\mathbf{x} + \frac{\rho_f}{2} \int_{\Omega^f(t^n)} (\nabla \cdot \mathbf{w}_k^{n+1}) \mathbf{v}_k^{n+1} \cdot \varphi_k d\mathbf{x} \\ & + \frac{\rho_f}{2} \int_{\Omega^f(t^n)} ((\mathbf{v}_k^n - \mathbf{w}_k^{n+1}) \cdot \nabla) \mathbf{v}_k^{n+1} \cdot \varphi_k - ((\mathbf{v}_k^n - \mathbf{w}_k^{n+1}) \cdot \nabla) \varphi_k \cdot \mathbf{v}_k^{n+1} \\ & + a_f^n(\mathbf{v}_k^{n+1}, \varphi_k) - b_f^n(p_k^{n+1}, \varphi_k) + b_f^n(q_k, \mathbf{v}_k^{n+1}) \\ & + \rho_m h \int_0^L \frac{\widehat{v_{r,k}^{n+1}|_{\Gamma(t^n)}} - \widehat{v_{r,k}^{n+1/2}|_{\Gamma(t^n)}}}{\Delta t} \varphi_{r,k} dx \\ & = \int_0^R p_{in}(t^{n+1}) \varphi_{z,k}|_{z=0} dr - \int_0^R p_{out}(t^{n+1}) \varphi_{z,k}|_{z=L} dr, \end{aligned} \quad (50)$$

where the initial data for the trace of the fluid velocity on  $\Gamma(t^n)$  comes from the just calculated velocity of the thin structure  $\widehat{v_{r,k}^{n+1/2}}|_{\Gamma(t^n)} = \hat{\xi}_{r,k}^{n+1/2}$ .

Then set  $\hat{\mathbf{U}}_k^{n+1} = \hat{\mathbf{U}}_k^{n+1/2}$ ,  $\hat{\mathbf{V}}_k^{n+1} = \hat{\mathbf{V}}_k^{n+1/2}$ ,  $\hat{\eta}_{r,k}^{n+1} = \hat{\eta}_{r,k}^{n+1/2}$ , and  $\hat{\xi}_{r,k}^{n+1} = \hat{\xi}_{r,k}^{n+1/2}$ .

The ALE velocity  $\mathbf{w}^{n+1}$  that appears in Problem **A2** is calculated after computing the new structure displacement in Problem **A1**. Note that Problem **A1** is the only step in which the displacement of the structure changes. Hence, after computing the new structure displacement in Problem **A1**,  $\hat{\eta}_{r,k}^n$  determines the “reference domain” and  $\hat{\eta}_{r,k}^{n+1/2}$ , which is the same as  $\hat{\eta}_{r,k}^{n+1}$ , determines the location of the new domain. To update the position of the fluid domain (after Problem **A2**), we consider the following simple ALE mapping:

$$A_{t^n} : \hat{\Omega}^f \rightarrow \Omega^f(t^n), \quad A_{t^n}(\hat{z}, \hat{r}) := \left( \hat{z}, \frac{R + \hat{\eta}_{r,k}^n}{R} \hat{r} \right)^\tau.$$

We will also need the explicit form of the ALE mapping from the computational domain  $\Omega^f(t^n)$  to  $\Omega^f(t^{n+1})$ , which is given by

$$A_{t^{n+1}} \circ A_{t^n}^{-1} : \Omega^f(t^n) \rightarrow \Omega^f(t^{n+1}), \quad A_{t^{n+1}} \circ A_{t^n}^{-1}(z, r) = \left( z, \frac{R + \hat{\eta}_{r,k}^{n+1}}{R + \hat{\eta}_{r,k}^n} r \right)^\tau.$$

The corresponding Jacobian and the ALE velocity are given, respectively, by

$$J_n^{n+1} := \frac{R + \hat{\eta}_{r,k}^{n+1}}{R + \hat{\eta}_{r,k}^n}, \quad \mathbf{w}_k^{n+1} = \frac{1}{\Delta t} \frac{\hat{\eta}_{r,k}^{n+1} - \hat{\eta}_{r,k}^n}{R + \hat{\eta}_{r,k}^n} r \mathbf{e}_r. \quad (51)$$

Therefore, the time-derivative of the interface displacement is approximated by  $(\hat{\eta}_{r,k}^{n+1} - \hat{\eta}_{r,k}^n)/\Delta t$ , which enters the expression for the ALE velocity  $\mathbf{w}^{n+1}$ .

#### 4.2. Stability analysis

Let  $\mathcal{E}_f^n$  denote the discrete energy of the fluid problem,  $\mathcal{E}_s^n$  the discrete energy of the structure problem, and let  $\mathcal{E}_m^n$  denote the discrete energy of the simplified membrane problem at time level  $n\Delta t$ :

$$\begin{aligned} \mathcal{E}_f^n &:= \frac{\rho_f}{2} \|\mathbf{v}_k^n\|_{L^2(\Omega^f(t^n))}^2, \\ \mathcal{E}_s^n &:= \frac{\rho_s}{2} \|\hat{\mathbf{V}}_k^n\|_{L^2(\hat{\Omega}^s)}^2 + \mu_s \|D(\hat{\mathbf{U}}_k^n)\|_{L^2(\hat{\Omega}^s)}^2 + \frac{\lambda_s}{2} \|\nabla \cdot \hat{\mathbf{U}}_k^n\|_{L^2(\hat{\Omega}^s)}^2 + \frac{\gamma}{2} \|\hat{\mathbf{U}}_k^n\|_{L^2(\hat{\Omega}^s)}^2, \\ \mathcal{E}_m^n &:= \frac{\rho_m h}{2} \|\hat{\xi}_{r,k}^n\|_{L^2(0,L)}^2 + \frac{C_0}{2} \|\hat{\eta}_{r,k}^n\|_{L^2(0,L)}^2. \end{aligned}$$

The following energy estimate holds for the full nonlinear FSI problem, satisfying assumptions **1** and **2** above.

**Theorem 1. (An energy estimate of the operator splitting scheme)**

Let  $\{(\mathbf{v}^n, \mathbf{U}^n, \mathbf{V}^n, \eta_r^n, \xi_r^n)\}_{0 \leq n \leq N}$  be a solution of (49)-(50). Then, the following energy estimate holds:

$$\begin{aligned} & \mathcal{E}_f^N + \mathcal{E}_s^N + \mathcal{E}_m^N + \frac{\rho_f}{2} \sum_{n=0}^{N-1} \|\mathbf{v}_k^{n+1} - \mathbf{v}_k^{n+1/2}\|_{L^2(\Omega^f(t^n))}^2 + \mu_f \Delta t \sum_{n=0}^{N-1} \|D(\mathbf{v}_k^{n+1})\|_{L^2(\Omega^f(t^n))}^2 \\ & \quad + \frac{\rho_m h}{2} \sum_{n=0}^{N-1} \|\widehat{v_{r,k}^{n+1}}|_{\Gamma(t^n)} - \widehat{v_{r,k}^{n+1/2}}|_{\Gamma(t^n)}\|_{L^2(0,L)}^2 \\ & \leq \mathcal{E}_f^0 + \mathcal{E}_s^0 + \mathcal{E}_m^0 + \frac{C}{\mu_f} \Delta t \sum_{n=0}^{N-1} \|p_{in}(t^n)\|_{L^2(0,R)}^2 + \frac{C}{\mu_f} \Delta t \sum_{n=0}^{N-1} \|p_{out}(t^n)\|_{L^2(0,R)}^2. \end{aligned}$$

This energy estimate shows that the total energy of the coupled discretized problem is bounded by the energy of the initial data, and by the work done by the inlet and outlet dynamic pressure data, independently of the time step, for all the parameters in the problem. Notice that the total energy of the problem includes the kinetic energy of the fluid and the kinetic energy of both structures, the elastic energy of both structures, and, additionally, the kinetic energy that is due to the motion of the fluid domain and of the fluid domain boundary. The last two contributions are accounted for in the two terms on the left hand-side of the energy inequality, containing the  $L^2$ -norms of the difference between the fluid velocities at times  $n+1$  and  $n+1/2$ .

*Proof.* To prove the energy estimate, we test the structure problem (49) with

$(\hat{\psi}_k, \hat{\phi}_k) = (\frac{\hat{\mathbf{U}}_k^{n+1/2} - \hat{\mathbf{U}}_k^n}{\Delta t}, \frac{\hat{\mathbf{V}}_k^{n+1/2} - \hat{\mathbf{V}}_k^n}{\Delta t})$ , and the fluid problem (50) with  $(\varphi_k, q_k) = (\mathbf{v}_k^{n+1}, p_k^{n+1})$ . With this choice of test functions, after multiplying by  $\Delta t$ , Problem **A1** reduces to

$$\begin{aligned} & \mathcal{E}_s^{n+1/2} + \frac{\rho_m h}{2} \|\hat{\xi}_{r,k}^{n+1/2}\|_{L^2(0,L)}^2 - \frac{\rho_m h}{2} \|\hat{\xi}_{r,k}^n\|_{L^2(0,L)}^2 + \frac{C_0}{2} \|\hat{\eta}_{r,k}^{n+1/2}\|_{L^2(0,L)}^2 \\ & \quad - \frac{C_0}{2} \|\hat{\eta}_{r,k}^n\|_{L^2(0,L)}^2 = \mathcal{E}_s^n. \end{aligned} \tag{52}$$

In Problem **A2**, after replacing the test functions by the fluid velocity  $\mathbf{v}_k^{n+1}$ , the symmetrized advection terms cancel out. To deal with the first term on the left in Problem **A2**, we use the identity

$$a(a-b) = \frac{1}{2}(a^2 - b^2 + (a-b)^2). \quad (53)$$

Then, the first two terms combined (fluid inertia) become

$$\begin{aligned} & \frac{\rho_f}{2} \frac{1}{\Delta t} \int_{\Omega^f(t^n)} \left( \left( 1 + \frac{\hat{\eta}_{r,k}^{n+1} - \hat{\eta}_{r,k}^n}{R + \hat{\eta}_{r,k}^n} \right) |\mathbf{v}_k^{n+1}|^2 + |\mathbf{v}_k^{n+1} - \mathbf{v}_k^{n+1/2}|^2 - |\mathbf{v}_k^{n+1/2}|^2 \right) d\mathbf{x} \\ &= \frac{\rho_f}{2} \frac{1}{\Delta t} \int_{\Omega^f(t^n)} \left( \frac{R + \hat{\eta}_{r,k}^{n+1}}{R + \hat{\eta}_{r,k}^n} |\mathbf{v}_k^{n+1}|^2 + |\mathbf{v}_k^{n+1} - \mathbf{v}_k^{n+1/2}|^2 - |\mathbf{v}_k^{n+1/2}|^2 \right) d\mathbf{x}. \end{aligned}$$

Note that, since the fluid does not change in Problem **A1**,  $\mathbf{v}_k^{n+1/2} = \mathbf{v}_k^n$ . Furthermore, notice that  $(R + \eta^{n+1})/(R + \eta^n)$  is exactly the Jacobian of the ALE mapping from  $\Omega^f(t^n)$  to  $\Omega^f(t^{n+1})$ , see (51), and so we can convert that integral into an integral over  $\Omega^f(t^{n+1})$  to recover the kinetic energy of the fluid at the next time-step:

$$\frac{\rho_f}{2} \frac{1}{\Delta t} \int_{\Omega^f(t^n)} \frac{R + \hat{\eta}_{r,k}^{n+1}}{R + \hat{\eta}_{r,k}^n} |\mathbf{v}_k^{n+1}|^2 d\mathbf{x} = \frac{\rho_f}{2} \frac{1}{\Delta t} \int_{\Omega^f(t^{n+1})} |\mathbf{v}_k^{n+1}|^2 d\mathbf{x}.$$

This calculation also shows that the ALE mapping and its Jacobian satisfy the geometric conservation law property, as studied by Farhat et al. in [22].

Therefore, after multiplying by  $\Delta t$ , the energy associated with Problem **A2** is given by

$$\begin{aligned} & \frac{\rho_f}{2} \|\mathbf{v}_k^{n+1}\|_{L^2(\Omega^f(t^{n+1}))}^2 - \frac{\rho_f}{2} \|\mathbf{v}_k^{n+1/2}\|_{L^2(\Omega^f(t^n))}^2 + \frac{\rho_f}{2} \|\mathbf{v}_k^{n+1} - \mathbf{v}_k^{n+1/2}\|_{L^2(\Omega^f(t^n))}^2 \\ & + 2\mu_f \Delta t \|D(\mathbf{v}_k^{n+1})\|_{L^2(\Omega^f(t^n))}^2 + \frac{\rho_m h}{2} \|\widehat{v_{r,k}^{n+1}}|_{\Gamma(t^n)}\|_{L^2(0,L)}^2 - \frac{\rho_m h}{2} \|\widehat{v_{r,k}^{n+1/2}}|_{\Gamma(t^n)}\|_{L^2(0,L)}^2 \\ & + \frac{\rho_m h}{2} \|\widehat{v_{r,k}^{n+1}}|_{\Gamma(t^n)} - \widehat{v_{r,k}^{n+1/2}}|_{\Gamma(t^n)}\|_{L^2(0,L)}^2 = \Delta t \int_0^R p_{in}(t^{n+1}) v_{z,k}^{n+1}|_{z=0} dr \\ & - \Delta t \int_0^R p_{out}(t^{n+1}) v_{z,k}^{n+1}|_{z=L} dr. \end{aligned} \quad (54)$$

Now, equations (52) and (54) are added, and the following properties are taken into account: first  $\widehat{v_{r,k}^{n+1/2}}|_{\Gamma(t^n)} = \hat{\xi}_{r,k}^{n+1/2}$ , and further, due to the

kinematic coupling condition we also have  $\widehat{v_{r,k}^{n+1}|_{\Gamma(t^n)}} = \hat{\xi}_{r,k}^{n+1}$ . After adding equations (52) and (54), and taking into account  $\mathcal{E}_s^{n+1/2} = \mathcal{E}_s^{n+1}$  since the displacement changes only in the first step, we get

$$\begin{aligned} & \mathcal{E}_f^{n+1} + \mathcal{E}_s^{n+1} + \mathcal{E}_m^{n+1} + \frac{\rho_f}{2} \|\mathbf{v}_k^{n+1} - \mathbf{v}_k^{n+1/2}\|_{L^2(\Omega^f(t^n))}^2 + 2\mu_f \Delta t \|D(\mathbf{v}_k^{n+1})\|_{L^2(\Omega^f(t^n))}^2 \\ & \quad + \frac{\rho_m h}{2} \|\widehat{v_{r,k}^{n+1}|_{\Gamma(t^n)}} - \widehat{v_{r,k}^{n+1/2}|_{\Gamma(t^n)}}\|_{L^2(0,L)}^2 \\ & = \mathcal{E}_f^n + \mathcal{E}_s^n + \mathcal{E}_m^n + \Delta t \int_0^R p_{in}(t^{n+1}) v_{z,k}^{n+1}|_{z=0} dr - \Delta t \int_0^R p_{out}(t^{n+1}) v_{z,k}^{n+1}|_{z=L} dr. \end{aligned}$$

To bound the right-hand side of this equality, we use the Cauchy-Schwartz and Young's inequalities

$$\begin{aligned} & \Delta t \int_0^R p_{in}(t^{n+1}) v_{z,k}^{n+1}|_{z=0} dr - \Delta t \int_0^R p_{out}(t^{n+1}) v_{z,k}^{n+1}|_{z=L} dr \\ & \leq \frac{\Delta t}{2\epsilon_1} \|p_{in}(t^n)\|_{L^2(0,R)}^2 + \frac{\Delta t}{2\epsilon_1} \|p_{out}(t^n)\|_{L^2(0,R)}^2 + \epsilon_1 \Delta t \|\mathbf{v}_k^{n+1}\|_{L^2(0,R)}^2. \end{aligned}$$

By the trace and Korn inequalities, we then have

$$\|\mathbf{v}_k^{n+1}\|_{L^2(0,R)}^2 \leq C \|D(\mathbf{v}_k^{n+1})\|_{L^2(\Omega^f(t^n))}^2,$$

where  $C$  is the constant from the trace and Korn inequalities. In general, Korn's constant depends on the domain. It was shown, however, that for domains associated with fluid-structure interaction problems of the type studied in this manuscript, the Korn's constant is independent of the sequence of approximating domains [62, 63].

By setting  $\epsilon_1 = \frac{\mu_f}{C}$ , the last term can be combined with the term on the left hand-side, associated with the fluid diffusion. Finally, summing the inequality from  $n = 0$  to  $N - 1$  we prove the desired energy estimate.  $\square$

Notice that our operator splitting algorithm consists of solving a set of sub-problems which are linear (elliptic). It was shown in [63] using compactness arguments, that the sequence of linear sub-problems converges to a weak solution of the full, nonlinear FSI problem with multilayered structures, in which the thin structure was modeled by the linear wave equation. The energy estimate, presented above, shows that the combined linear discretized sub-problems are stable, and that the sequence of approximate solutions to the nonlinear FSI problem is uniformly bounded in the corresponding energy norms.

Numerical results are presented next, where two instructive numerical examples are solved using the proposed scheme. The first example presents a simplified FSI problem with two layers, for which an exact solution was found and compared with the numerically calculated solution. The second example concerns a full, nonlinear FSI problem with two structural layers in which the thickness of the thin layer is taken to converge to zero. It was shown that the final solution compares well with the solution of the limiting FSI problem, obtained using a different computational solver from the one presented in this manuscript. Both examples show that the scheme is unconditionally stable, and that it converges to a solution of the underlying problem.

## 5. Numerical example 1: A simplified FSI problem with exact solution.

We consider a simplified FSI problem with multiple structural layers that satisfies the following simplifying assumptions:

1. The fluid problem is defined on the fixed, reference domain of width  $R$ , and length  $L$  (the coupling is linear).
2. The fluid problem is driven by the constant inlet and outlet pressure data  $p_{in}$  and  $p_{out} = 0$  (the pressure drop is constant).
3. Only radial displacement of the thin and thick structure is assumed to be different from zero.

Assumption 3 implies that the thin structure membrane model takes the form:

$$\rho_K h \frac{\partial^2 \eta_r}{\partial t^2} + C_0 \eta_r = f_r,$$

while the thick structure problem simplifies as follows:

$$\rho_s \frac{\partial^2 d_r}{\partial t^2} = \mu \frac{\partial^2 d_r}{\partial x^2} + (\mu + \lambda) \frac{\partial^2 d_r}{\partial y^2}.$$

Finally, the coupling conditions between the fluid and the multilayered structure are given by

$$\begin{aligned} f_r &= p + (\lambda + \mu) \frac{\partial d_r}{\partial y} && \text{on } \Gamma \times (0, T), \\ \frac{\partial \eta_r}{\partial t} &= u_r && \text{on } \Gamma \times (0, T), \\ \eta_r &= U_r && \text{on } \Gamma \times (0, T). \end{aligned}$$



The exact solution to this problem is given by the following. The fluid flow through the fixed cylinder with constant pressure drop is given by the Poiseuille velocity profile:

$$u_z^e(z, r) = u_z^e(r) = \frac{p_{in} - p_{out}}{2\mu_F L}(R^2 - r^2), \quad u_r^e = 0,$$

and the fluid pressure is linear within the channel:

$$p^e(z, r) = p^e(z) = \frac{p_{out}z + p_{in}(L - z)}{L}, \quad z \in (0, L), \quad r \in (0, R).$$

The radial displacements of the thin and thick structure are given by:

$$\eta_r^e(z) = \frac{p^e(z)}{C_0}, \quad d_r^e(z, r) = d_r^e(z) = \eta_r^e(z).$$

Parameters	Values	Parameters	Values
<b>Radius</b> $R$ (cm)	0.5	<b>Length</b> $L$ (cm)	6
<b>In. press.</b> $p_{in}$ (dyne/cm <sup>2</sup> )	250	<b>Out. press.</b> $p_{out}$ (dyne/cm <sup>2</sup> )	0
<b>Fluid density</b> $\rho_f$ (g/cm <sup>3</sup> )	1	<b>Dyn. viscosity</b> $\mu$ (g/cm s)	0.35
<b>Thin wall:</b>			
<b>Density</b> $\rho_m$ (g/cm <sup>3</sup> )	1.1	<b>Thickness</b> $h$ (cm)	0.02
<b>Lamé coeff.</b> $\mu_m$ (dyne/cm <sup>2</sup> )	$1.07 \times 10^6$	<b>Lamé coeff.</b> $\lambda_m$ (dyne/cm <sup>2</sup> )	$4.29 \times 10^6$
<b>Thick wall:</b>			
<b>Density</b> $\rho_s$ (g/cm <sup>3</sup> )	1.1	<b>Thickness</b> $H$ (cm)	0.1
<b>Lamé coeff.</b> $\mu_s$ (dyne/cm <sup>2</sup> )	$1.07 \times 10^6$	<b>Lamé coeff.</b> $\lambda_s$ (dyne/cm <sup>2</sup> )	$4.29 \times 10^6$
<b>Spring coeff.</b> $\gamma$ (dyne/cm <sup>4</sup> )	0		

Table 1: Geometry, fluid and structure parameters used in Example 1.

We solve this problem numerically using the parameters given in Table 1. The initial data was taken to be

$$\mathbf{u} = 0, p = p_{out}, \eta_r = 0, d_r = 0, \text{ at } t = 0,$$

while at the inlet and outlet boundaries we kept both structures fixed, with the inlet and outlet displacement data tailored so that the final solution does not exhibit a boundary layer:

$$\eta_r|_{z=0} = d_r|_{z=0} = \frac{p_{in}}{C_0}, \quad \eta_r|_{z=L} = d_r|_{z=L} = \frac{p_{out}}{C_0} = 0, \forall t > 0.$$

The numerical scheme with  $\beta = 1$  was implemented, and the problem was solved until the steady state was achieved. With the time step  $\Delta t = 10^{-5}$  it took 200 iterations to achieve the accuracy of less than 0.08%. Namely, the maximum relative error between the computed and exact solution was less than 0.08% (namely, 0.000778).

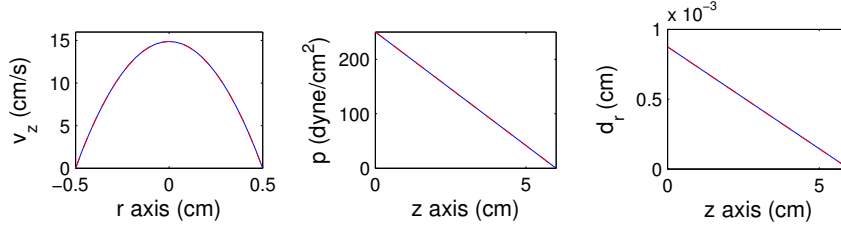


Figure 3: Comparison between the computed solution (in blue) and the exact solution (in red). The two are superimposed. Left: Axial velocity. Middle: Fluid pressure. Right: Radial displacement.

Figure 3 shows a comparison between the computed (blue) and the exact solution (red) for axial velocity (left), fluid pressure (middle), and radial displacement (right), showing excellent agreement. The corresponding relative errors are given by the following:

$$\begin{aligned} \frac{\|\mathbf{u}^e - \mathbf{u}\|_{L^2(\Omega^f)}}{\|\mathbf{u}^e\|_{L^2(\Omega^f)}} &= 7.78 \times 10^{-4}, & \frac{\|p^e - p\|_{L^2(\Omega^f)}}{\|p^e\|_{L^2(\Omega^f)}} &= 1.17 \times 10^{-4}, \\ \frac{\|\eta_r^e - \eta_r\|_{L^2(0,L)}}{\|\eta_r^e\|_{L^2(0,L)}} &= 3.82 \times 10^{-5}, & \frac{\|d_r^e - d_r\|_{L^2(\Omega^s)}}{\|d_r^e\|_{L^2(\Omega^s)}} &= 3.82 \times 10^{-5}. \end{aligned}$$

We conclude that the scheme behaves well for this simplified FSI problem with multiple structural layers.

## 6. Numerical example 2: A fully nonlinear FSI problem.

In this example we solve the full, nonlinear FSI problem (1)-(16). In this example the structure consists of two layers, one with thickness  $h$  (thin) and one with thickness  $H > h$  (thick). The combined thickness of the composite structure is  $h+H = 0.12\text{cm}$ . The data and parameters used in the simulation correspond to those used in [14] and [5] to test different FSI solvers. They are given in Table 2.

Parameters	Values	Parameters	Values
<b>Radius</b> $R$ (cm)	0.5	<b>Length</b> $L$ (cm)	6
<b>Fluid density</b> $\rho_f$ (g/cm <sup>3</sup> )	1	<b>Dyn. viscosity</b> $\mu$ (g/cm s)	0.035
<b>Thin wall:</b>			
<b>Density</b> $\rho_m$ (g/cm <sup>3</sup> )	1.1	<b>Thickness</b> $h$ (cm)	0.02
<b>Lamé coeff.</b> $\mu_m$ (dyne/cm <sup>2</sup> )	$5.75 \times 10^5$	<b>Lamé coeff.</b> $\lambda_m$ (dyne/cm <sup>2</sup> )	$1.7 \times 10^6$
<b>Thick wall:</b>			
<b>Density</b> $\rho_s$ (g/cm <sup>3</sup> )	1.1	<b>Thickness</b> $H$ (cm)	0.1
<b>Lamé coeff.</b> $\mu_s$ (dyne/cm <sup>2</sup> )	$5.75 \times 10^5$	<b>Lamé coeff.</b> $\lambda_s$ (dyne/cm <sup>2</sup> )	$1.7 \times 10^6$
<b>Spring coeff.</b> $\gamma$ (dyne/cm <sup>4</sup> )	$4 \times 10^6$		

Table 2: Geometry, fluid and structure parameters that are used in Example 2.

Since there are no benchmark results in FSI literature containing a two-layered composite structure interacting with an incompressible, viscous fluid, we take the following approach to test our FSI solver. We solve a sequence of FSI problems (1)-(16) in which the thickness of the thin layer converges to zero,  $h \rightarrow 0$ , while the combined thickness  $h + H$  remains fixed, and equal to 0.12cm. First, we proved, analytically, that the limiting functions (displacement and velocity) satisfy the FSI problem containing a single, thick structure, with thickness 0.12cm. This is presented in the Appendix. Then we numerically compare the “limiting” solution of the sequence of FSI problems with composite structures, obtained using the FSI solver proposed in this manuscript, with a solution of the FSI problem containing a single, thick structure with thickness  $h + H = 0.12$ cm, obtained using a different computational solver, namely a solver developed in [14]. We show that the two are in excellent agreement.

The elastodynamics of the thin structural layer is modeled using the linearly elastic Koiter membrane equations with both radial and longitudinal displacement (6), (7), while the elastodynamics of the thick structure is modeled using the equations of 2D linear elasticity (9).

The flow is driven by the time-dependent pressure data:

$$p_{in}(t) = \begin{cases} \frac{p_{max}}{2} \left[ 1 - \cos\left(\frac{2\pi t}{t_{max}}\right) \right] & \text{if } t \leq t_{max} \\ 0 & \text{if } t > t_{max} \end{cases}, \quad p_{out}(t) = 0 \quad \forall t \in (0, T),$$

where  $p_{max} = 1.333 \times 10^4$  (dyne/cm<sup>2</sup>) and  $t_{max} = 0.003$  (s).

The kinematically-coupled  $\beta$  scheme, described in Sections 2 and 3, was used to solve the multi-layered FSI problem with  $\beta = 1$ , while the scheme presented in [14] was used to solve the single-layered FSI benchmark problem with thick structure. The problem was solved over the time interval

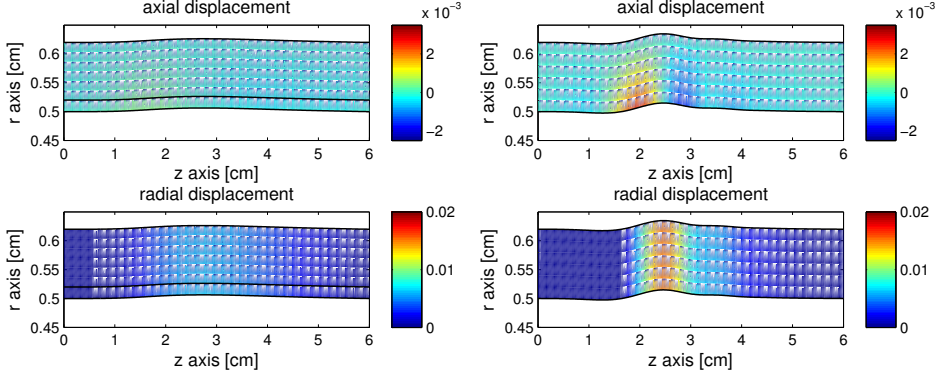


Figure 4: Axial displacement (top) and radial displacement (bottom) at time  $t = 8$  ms obtained using the model capturing two structural layers (left), and the model capturing FSI with a single thick structural layer [14] (right).

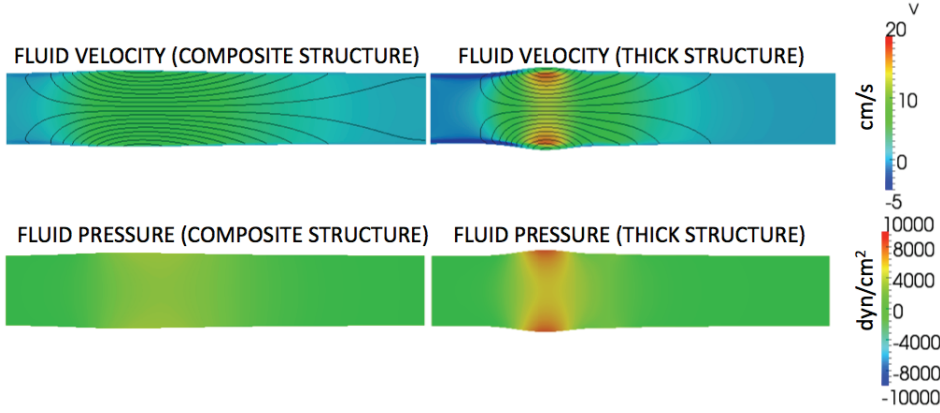


Figure 5: Fluid velocity (top) and fluid pressure (bottom) at time  $t = 8$  ms obtained using the model capturing two structural layers (left), and the model capturing FSI with a single thick structural layer [14] (right).

$[0, 0.012]$ s, using the time step  $\Delta t = 5 \times 10^{-5}$ . Figure 4 shows the axial and radial displacement at time  $t = 8$  ms obtained using the multilayered model (left) and the single-layered model (right) for the arterial wall. Figure 5 shows the corresponding fluid velocity and pressure. One can notice significant smoothing of both the displacement as well as the fluid velocity and pressure in the composite, i.e., multi-layered structure case. Same data are used for both simulations. We further compared the results of the multilayered model with the single layered model as the thickness of the thin

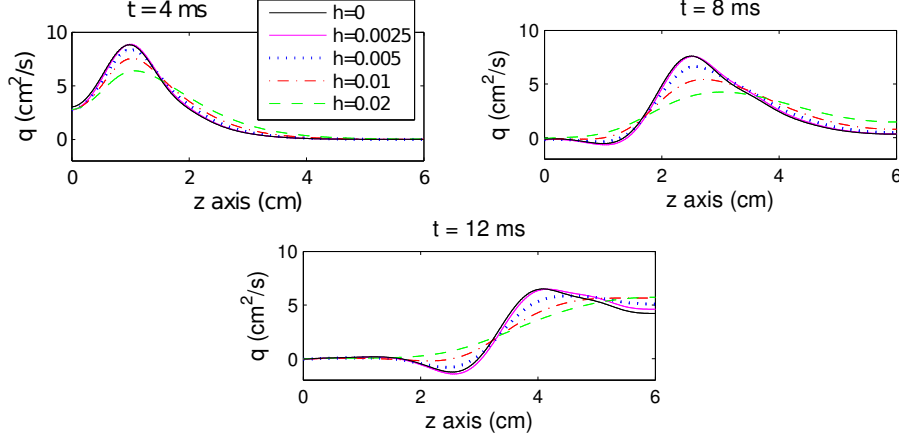


Figure 6: Flowrate computed using two different models: the model in [14] containing a single thick structural layer ( $h = 0$ ), and the model considered in this manuscript, consisting of two layers. The thickness of the thin membrane layer was decreased from  $h = 0.02$  to  $h = 0.0025$  cm. The combined thickness of the two-layered composite structure was kept constant at  $h + H = 0.12$  cm. Convergence of the solutions to the FSI solution containing a single, thick structure ( $h = 0$ ) can be observed.

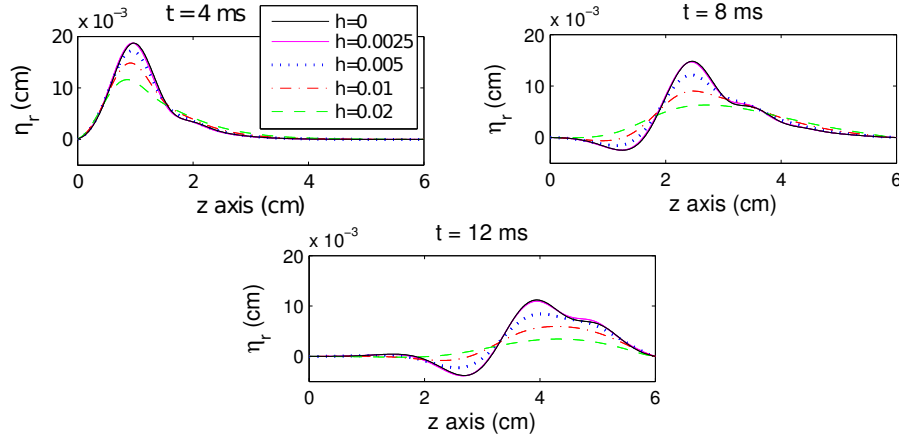


Figure 7: Displacement of the fluid-structure interface obtained under the same conditions as those described in Figure 6.

structure  $h$  goes to zero. As we decreased  $h$ , we increased  $H$  to maintain the constant combined thickness  $h + H = 0.12$  cm. Figures 6, 7 and 8 show the flowrate, mean pressure and displacement of the fluid-structure interface obtained using different values of  $h$ . The results obtained using the single layered wall model correspond to the label  $h = 0$ . Indeed, we can see that as

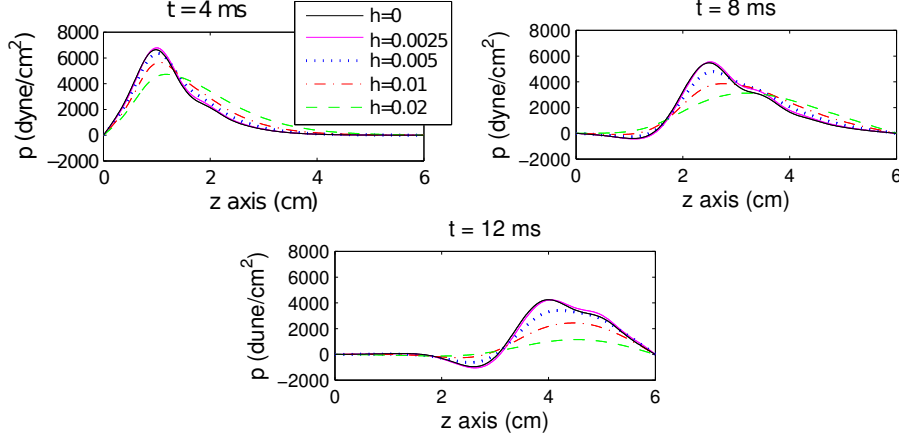


Figure 8: Mean pressure obtained under the same conditions as those described in Figure 6.

we decrease the thickness of the fluid-structure interface, the numerical results obtained using our multilayered model, approach the results obtained using the single-layered FSI model! Notice how for  $h = 0.025\text{cm}$  the solutions obtained using the multilayered model and the single thick structure model ( $h = 0$  in Figures 6, 7, 8) are almost identical.

We conclude this section by showing the log-log plots of computational error versus time discretization step, presented in Figure 9. The red line in the plots indicates the slope associated with 1st-order accuracy. We see that our computational solver is 1st-order accurate in time for structure displacement calculations, while producing higher order temporal accuracy for fluid pressure and velocity.

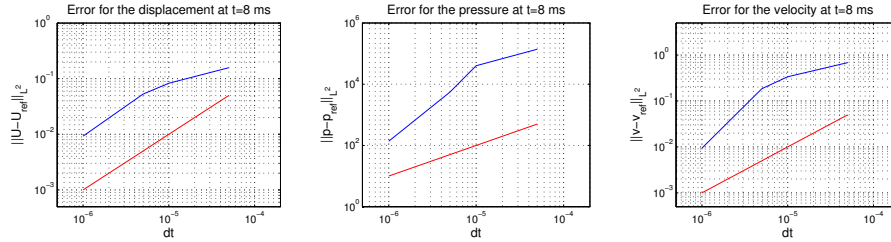


Figure 9: The  $L^2$ -norm error of the structure displacement, fluid pressure and velocity vs. time step, shown in the log-log plots. The red line shows the slope associated with first-order accuracy. We see 1st-order accuracy for displacement, and higher-order accuracy for pressure and velocity.

### 6.1. Regularizing Effects by Thin Fluid-Structure Interface with Mass

We conclude this section with a remark on the regularizing effects of the thin fluid-structure interface with mass. Figures 6, 7, 8 indicate that as we increase inertia of the thin fluid-structure interface with mass by increasing its thickness, the solution of the entire FSI problem is damped, or regularized. More precisely, if one looks at the FSI problem with a single thick structural layer, the fluid-structure interface is simply the massless trace of the thick structure that is in contact with the fluid. Mathematically, in that case the trace of the structure displacement is not well-defined (assuming regularity of the data consistent with weak solutions), and using energy estimates it is not possible to even show that the fluid-structure interface is continuous. In the case when the fluid-structure interface has mass, it was shown in [63] that not only is the fluid-structure interface continuous, but its evolution can be controlled by the energy norm of the time derivative of its displacement. We see effects of this in the solutions presented in Figures 6, 7, 8, and in Figures 10 below. In Figure 10 below we focus on the displacement and displacement velocity of the fluid-structure interface, which measures the effects of inertia. In the first row of Figure 10 three snap-shots

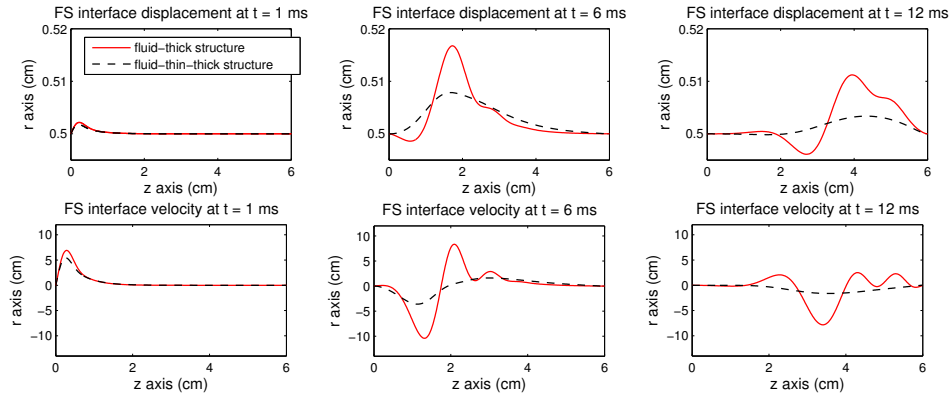


Figure 10: Fluid-structure interface displacement (top) and velocity (bottom) obtained using the multilayered wall model discussed in the present manuscript, and the single layered model from [14], shown at times  $t = 1$  ms,  $t = 6$  ms, and  $t = 12$  ms.

of the fluid-structure interface are shown as the inlet pressure wave travels down the tube. In the second row of Figure 10 the same three snap-shots are shown, but for the fluid-structure interface velocity. The red solid line in these figures corresponds to the massless fluid-structure interface in the FSI problem with a single thick structural layer. The black dashed line correspond to the fluid-structure interface with mass in the FSI problem with

two structural layers. We see significant damping of the traveling wave in the case when the fluid-structure interface has mass. This indicates that inertia of the fluid-structure interface with mass regularizes solutions of FSI problems.

This is reminiscent of the results by Hansen and Zuazua [40] in which the presence of point mass at the interface between two linearly elastic strings with solutions in asymmetric spaces (different regularity on each side) allowed the proof of well-posedness due to the regularizing effects by the point mass. In particular, in [40] two linearly elastic strings were considered, meeting at a point mass. The elastodynamics of each string was modeled by the linear wave equation. It was shown that as the wave with the displacement in  $H^1(0, L)$  and velocity in  $L^2(0, L)$  passes through the point mass, a reflected and a transmitted wave forms. The transmitted wave, which passes through the point mass, gets smoothed out to  $H^2(0, L)$  regularity in displacement, and  $H^1(0, L)$  regularity in velocity. A numerical simulation of this phenomenon was shown in [50]. Figure 11 shows one of the results

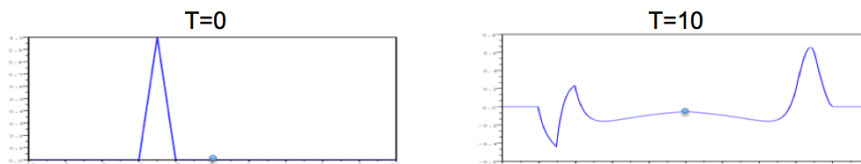


Figure 11: Regularizing effects of point mass. The figure is taken from [50]. The initial data (left panel) is smoothed out as the transmitted wave traveling to the right, passes through the point mass (right panel).

from [50]. The panel on the left shows the initial displacement in  $H^1(0, L)$  with zero initial velocity, located just left from the point mass. The panel on the right shows the solution at time  $T = 10s$  at which the reflected and transmitted waves have formed, with the displacement of the reflected wave on the left of the point mass still in  $H^1(0, L)$ , but with the displacement of the transmitted wave, shown to the right of the point mass, belonging to  $H^2(0, L)$ . For a reader with further interest in the area of simplified coupled problems we mention [44, 71, 76].

## 7. Appendix: Proof of convergence as $h \rightarrow 0$ of FSI solutions with composite structures to a FSI solution with a single thick structure.

We consider here the original FSI problem (1)-(16) satisfying the following simplifying assumptions:



1. The fluid problem is defined on a fixed fluid domain  $\Omega^f$  (linear coupling).
2. Fluid advection is neglected leading to a time-dependent Stokes problem for the fluid.

In this case the coupled FSI problem with composite structure consisting of a thick structure sitting on top of a thin membrane with thickness  $h$ , serving as a fluid-structure interface with mass, takes the following form:

$$\left. \begin{aligned} \varrho_f \partial_t \mathbf{v}^h &= \nabla \cdot \boldsymbol{\sigma}^f(\mathbf{v}^h, p^h) \\ \nabla \cdot \mathbf{v}^h &= 0 \end{aligned} \right\} \text{ in } \Omega^f \times (0, T), \quad (55)$$

$$\rho_s \partial_t^2 \mathbf{U}^h + \gamma \mathbf{U}^h = \nabla \cdot \boldsymbol{\sigma}^s(\mathbf{U}^h) \text{ in } \Omega^s \times (0, T), \quad (56)$$

$$\left. \begin{aligned} \rho_m h \partial_t^2 \eta_z^h - C_2(h) \partial_z \eta_r^h - C_1(h) \partial_z^2 \eta_z^h &= -\boldsymbol{\sigma}^f \mathbf{n} \cdot \mathbf{e}_z + S \mathbf{n} \cdot \mathbf{e}_z \\ \rho_m h \partial_t^2 \eta_r^h + C_0(h) \eta_r^h + C_2(h) \partial_z \eta_z^h &= -\boldsymbol{\sigma}^f \mathbf{n} \cdot \mathbf{e}_r + S \mathbf{n} \cdot \mathbf{e}_r \\ \mathbf{v}^h &= \partial_t \boldsymbol{\eta}^h \end{aligned} \right\} \text{ on } \Gamma \times (0, T), \quad (57)$$

$$\boldsymbol{\sigma} \mathbf{n}_{in}^f = -p_{in}(t) \mathbf{n}_{in}^f \text{ on } \Gamma_{in}^f \times (0, T), \quad (58)$$

$$\boldsymbol{\sigma} \mathbf{n}_{out}^f = -p_{out}(t) \mathbf{n}_{out}^f \text{ on } \Gamma_{out}^f \times (0, T), \quad (59)$$

where the coefficients  $C_i(h)$ ,  $i = 0, 1, 2$ , all depend on  $h$  and are given by formulas (8). The super-script  $h$  in  $\mathbf{v}^h$  refers to a solution of the FSI problem with composite structure in which  $h$  denotes the thickness of the fluid-structure interface with mass. Equations (55)-(59) are supplemented with initial and boundary data. This gives rise to a well-defined *linear* FSI problem.

The weak formulation of problem (55)-(59) is given by:

$$\begin{aligned}
& -\varrho_f \int_0^T \int_{\Omega^f} \mathbf{v}^h \cdot \partial_t \boldsymbol{\varphi} + 2\mu_f \int_0^T \int_{\Omega^f} \mathbf{D}(\mathbf{v}^h) : \mathbf{D}(\boldsymbol{\varphi}) - \varrho_m h \int_0^T \int_{\Gamma} \partial_t \eta_r^h \partial_t \zeta_r \\
& - \varrho_m h \int_0^T \int_{\Gamma} \partial_t \eta_z^h \partial_t \zeta_z + C_2(h) \int_0^T \int_{\Gamma} (\partial_z \eta_z^h \zeta_r - \partial_z \eta_r^h \zeta_z) + C_1(h) \int_0^T \int_{\Gamma} \partial_z \eta_z^h \partial_z \zeta_z \\
& + C_0(h) \int_0^T \int_{\Gamma} \eta_r^h \zeta_r - \varrho_s \int_0^T \int_{\Omega^s} \partial_t \mathbf{U}^h \cdot \partial_t \boldsymbol{\psi} + 2\mu_s \int_0^T \int_{\Omega^s} \mathbf{D}(\mathbf{U}^h) : \mathbf{D}(\boldsymbol{\psi}) \\
& + \lambda_s \int_{\Omega^s} (\nabla \cdot \mathbf{U}^h)(\nabla \cdot \boldsymbol{\psi}) + \gamma \int_0^T \int_{\Omega^s} \mathbf{U}^h \cdot \boldsymbol{\psi} = \pm \int_0^T \int_{\Gamma_{in/out}^f} p_{in/out}(t) \varphi_z \\
& + \rho_f \int_{\Omega^f} \mathbf{v}_0 \cdot \boldsymbol{\varphi}(0) + \rho_m h \int_{\Gamma} \partial_t \eta(0) \zeta(0) + \rho_s \int_{\Omega^s} \mathbf{V}_0 \cdot \boldsymbol{\psi}(0),
\end{aligned} \tag{60}$$

for all  $(\boldsymbol{\varphi}, \zeta, \boldsymbol{\psi}) \in C_c^1(0, T; V^f(\Omega^f) \times H_0^1(0, L)^2 \times U^s(\Omega^s))$ , such that  $\boldsymbol{\varphi}|_{\Gamma} = \zeta = \boldsymbol{\psi}|_{\Gamma}$ , where

$$\begin{aligned}
V^f &= \{\boldsymbol{\varphi} \in H^1(\Omega^f)^2 \mid \varphi_r|_{r=0} = 0, \boldsymbol{\varphi}|_{z=0, L} = 0\}, \\
U^s &= \{\boldsymbol{\varphi} \in H^1(\Omega^s)^2 \mid \psi_z|_{\Gamma_{ext}} = 0, \boldsymbol{\psi}|_{z=0, L} = 0\}.
\end{aligned}$$

and  $C_0(h)$ ,  $C_1(h)$ , and  $C_2(h)$  are given by (8).

It is easy to see that for every  $h > 0$  there exists a weak solution  $(\mathbf{v}^h, \boldsymbol{\eta}^h, \mathbf{U}^h)$  to problem (55)-(59) satisfying the following energy inequality:

$$\begin{aligned}
& \varrho_f \|\mathbf{v}^h\|_{L^\infty([0, T]; L^2(\Omega^f))}^2 + \mu_f \|\mathbf{D}(\mathbf{v}^h)\|_{L^2(0, T; L^2(\Omega^f))}^2 + \varrho_m h \|\partial_t \boldsymbol{\eta}^h\|_{L^\infty(0, T; L^2(\Gamma))}^2 \\
& h \left( 4\mu_m \left\| \frac{\eta_r^h}{R} \right\|_{L^2(0, L)}^2 + 4\mu_m \|\partial_z \eta_z^h\|_{L^2(0, L)}^2 + \frac{4\mu_m \lambda_m}{\lambda_m + 2\mu_m} \|\partial_z \eta_z^h + \frac{\eta_r^h}{R}\|_{L^2(0, L)}^2 \right) \\
& + \varrho_s \|\partial_t \mathbf{U}^h\|_{L^\infty(0, T; L^2(\Omega^s))}^2 + C(\mu_s, \lambda_s, \gamma) \|\mathbf{U}^h\|_{L^2(0, T; H^1(\Omega^s))}^2 \\
& \leq C(P_{in}, P_{out}, \mathbf{v}_0, \mathbf{V}_0, \eta_0).
\end{aligned} \tag{61}$$

Since the right hand side of this energy inequality does not depend on  $h$ , the sequence of solutions of problems (55)-(59), defined for different values of  $h$ , is uniformly bounded. From here, the following weak and weak\* convergence

results hold as  $h \rightarrow 0$ :

$$\begin{aligned}
\mathbf{v}^h &\rightharpoonup \mathbf{v} \quad \text{weak*} \quad \text{in } L^\infty(0, T; L^2(\Omega^f)), \\
\mathbf{v}^h &\rightharpoonup \mathbf{v} \quad \text{weak} \quad \text{in } L^2(0, T; H^1(\Omega^f)), \\
\mathbf{U}^h &\rightharpoonup \mathbf{U} \quad \text{weak} \quad \text{in } L^2(0, T; H^1(\Omega^s)), \\
\partial_t \mathbf{U}^h &\rightharpoonup \partial_t \mathbf{U} \quad \text{weak*} \quad \text{in } L^\infty(0, T; L^2(\Omega^s)), \\
\sqrt{h} \boldsymbol{\eta}^h &\rightharpoonup \boldsymbol{\eta} \quad \text{weak} \quad \text{in } L^2(0, T; L^2(\Gamma))^2, \\
\sqrt{h} \partial_t \boldsymbol{\eta}^h &\rightharpoonup \boldsymbol{\eta}_1 \quad \text{weak*} \quad \text{in } L^\infty(0, T; L^2(\Gamma))^2, \\
\sqrt{h} \partial_z \eta_z^h &\rightharpoonup \eta_2 \quad \text{weak*} \quad \text{in } L^\infty(0, T; L^2(\Gamma)).
\end{aligned} \tag{62}$$

From the uniqueness of the limit in  $\mathcal{D}'(\Gamma)$  we conclude that  $\boldsymbol{\eta}_1 = \partial_t \boldsymbol{\eta}$ , and  $\eta_2 = \partial_z \eta_z$ .

What is left is to identify the limits  $\boldsymbol{\eta}$  and  $\partial_t \boldsymbol{\eta}$ . From the kinematic coupling condition and the Trace Theorem we have:

$$\|\partial_t \boldsymbol{\eta}^h\|_{L^2([0, T]; L^2(\Gamma))} = \|\mathbf{v}^h\|_{L^2(0, T; L^2(\Gamma))} \leq \|\mathbf{v}^h\|_{L^2(0, T; H^1(\Omega^f))} \leq C,$$

where  $C$  is independent of  $h$ . From the uniform boundedness of  $\|\partial_t \boldsymbol{\eta}^h\|_{L^2(0, T; L^2(\Gamma))}$  we have

$$\sqrt{h} \partial_t \boldsymbol{\eta}^h \rightarrow 0 \quad \text{in } L^2(0, T; L^2(\Gamma)).$$

Uniqueness of the limit in  $\mathcal{D}'(\Gamma)$  implies  $\partial_t \boldsymbol{\eta} = 0$ . Similarly, we get  $\boldsymbol{\eta} = 0$  using the fact that  $\boldsymbol{\eta}^h(s, \cdot) = \eta_0 + \int_0^s \partial_t \boldsymbol{\eta}^h$ .

We can now pass to the limit as  $h \rightarrow 0$  in the linear problem (60)-(59) by using (62) to get the following equality:

$$\begin{aligned}
& -\varrho_f \int_0^T \int_{\Omega^f} \mathbf{v} \cdot \partial_t \boldsymbol{\varphi} + 2\mu_f \int_0^T \int_{\Omega^f} \mathbf{D}(\mathbf{v}) : \mathbf{D}(\boldsymbol{\varphi}) - \varrho_s \int_0^T \int_{\Omega^s} \partial_t \mathbf{U} \cdot \partial_t \boldsymbol{\psi} \\
& + 2\mu_s \int_0^T \int_{\Omega^s} \mathbf{D}(\mathbf{U}) : \mathbf{D}(\boldsymbol{\psi}) + \lambda_s \int_{\Omega^s} (\nabla \cdot \mathbf{U})(\nabla \cdot \boldsymbol{\psi}) + \gamma \int_0^T \int_{\Omega^s} \mathbf{U} \cdot \boldsymbol{\psi} \\
& = \pm \int_0^T \int_{\Gamma_{in/out}^f} p_{in/out}(t) \varphi_z + \rho_f \int_{\Gamma} \mathbf{v}_0 \boldsymbol{\zeta}(0) + \rho_s \int_{\Omega^s} \mathbf{V}_0 \cdot \boldsymbol{\psi}(0),
\end{aligned} \tag{63}$$

for all  $(\boldsymbol{\phi}, \boldsymbol{\psi}) \in C_c^1([0, T]; V^f(\Omega^f) \times U^s(\Omega^s))$  such that  $\boldsymbol{\phi}|_{\Gamma} = \boldsymbol{\psi}|_{\Gamma}$ . This shows that the limiting functions satisfy the weak form of the FSI with a single, thick elastic structure, coupled to the motion of an incompressible, viscous fluid via a mass-less fluid-structure interface.

**Remark 2.** We did not have to identify the limit  $\boldsymbol{\eta}$  in order to pass to the limit. Namely, we have:

$$\varrho_m h \partial_t \boldsymbol{\eta}^h = \sqrt{\varrho_m h} (\sqrt{\varrho_m h} \partial_t \boldsymbol{\eta}^h) \rightharpoonup \sqrt{\varrho_m h} \partial_t \boldsymbol{\eta} = 0.$$

## 8. Acknowledgements

Research of Bukač was partially supported by NSF via grant DMS-1318763. Research of Čanić was partially supported by NSF via grants NIGMS DMS-1263572, DMS-1318763, DMS-1311709, DMS-1262385 and DMS-1109189. Research of Muha was partially supported by NSF via grant DMS-1311709.

## References

- [1] M. Astorino, F. Chouly, and M.A. Fernández. An added-mass free semi-implicit coupling scheme for fluid-structure interaction. *Comptes Rendus Mathématique*, 347(1-2):99–104, 2009.
- [2] M. Astorino, F. Chouly, and M.A. Fernández Varela. Robin based semi-implicit coupling in fluid-structure interaction: Stability analysis and numerics. *SIAM J. Sci. Comput.*, 31:4041–4065, 2009.
- [3] F.P.T. Baaijens. A fictitious domain/mortar element method for fluid-structure interaction. *Int. J. Numer. Meth. Fl.*, 35(7):743–761, 2001.
- [4] S. Badia, F. Nobile, and C. Vergara. Fluid-structure partitioned procedures based on Robin transmission conditions. *J. Comput. Phys.*, 227:7027–7051, 2008.
- [5] S. Badia, F. Nobile, and C. Vergara. Fluid-structure partitioned procedures based on Robin transmission conditions. *J. Comput. Phys.*, 227(14):7027–7051, 2008.
- [6] S. Badia, F.. Nobile, and C. Vergara. Robin-Robin preconditioned Krylov methods for fluid-structure interaction problems. *Comput. Methods Appl. Mech. Eng.*, 198(33-36):2768–2784, 2009.
- [7] S. Badia, A. Quaini, and A. Quarteroni. Splitting methods based on algebraic factorization for fluid-structure interaction. *SIAM J. Sci. Comput.*, 30(4):1778–1805, 2008.
- [8] A.T. Barker and X.C. Cai. Scalable parallel methods for monolithic coupling in fluid-structure interaction with application to blood flow modeling. *Journal of Computational Physics*, 229(3):642–659, 2010.
- [9] Y. Bazilevs, V.M. Calo, Hughes T.J.R., and Y. Zhang. Isogeometric fluid-structure interaction: theory algorithms and computations. *Comput. Mech.*, 43:3–37, 2008.

- [10] Y. Bazilevs, V.M. Calo, Y. Zhang, and Hughes T.J.R. Isogeometric fluid-structure interaction analysis with applications to arterial blood flow. *Comput. Mech.*, 38(4-5):310–322, 2006.
- [11] M. Bukač, S. Čanić, R. Glowinski, J. Tambača, and A. Quaini. Fluid-structure interaction in blood flow capturing non-zero longitudinal structure displacement. *Journal of Computational Physics*, 2012.
- [12] M. Bukač, P. Zunino, and I. Yotov. Explicit partitioning strategies for interaction of the fluid with a multilayered poroelastic structure: An operator-splitting approach. *In preparation*, 2013.
- [13] M. Bukač and S. Čanić. Longitudinal displacement in viscoelastic arteries: a novel fluid-structure interaction computational model, and experimental validation. *Journal of Mathematical Biosciences and Engineering*, (10(2)):258–388, 2013.
- [14] M. Bukač, S. Čanić, R. Glowinski, B. Muha, and A. Quaini. A modular, operator splitting scheme for fluid-structure interaction problems with thick structures. *International Journal for Numerical Methods in Fluids*, Accepted 2013.
- [15] E. Burman and M.A. Fernández. Stabilization of explicit coupling in fluid-structure interaction involving fluid incompressibility. *Comput. Methods Appl. Mech. Eng.*, 198:766–784, 2009.
- [16] P. Causin, J.F. Gerbeau, and F. Nobile. Added-mass effect in the design of partitioned algorithms for fluid-structure problems. *Comput. Methods Appl. Mech. Eng.*, 194(42-44):4506–4527, 2005.
- [17] G.H. Cottet, E. Maitre, and T. Milcent. Eulerian formulation and level set models for incompressible fluid-structure interaction. *Esaim. Math. Model. Numer. Anal.*, 42:471–492, 2008.
- [18] S. Deparis, M. Discacciati, G. Foullet, and A. Quarteroni. Fluid-structure algorithms based on Steklov-Poincaré operators. *Comput. Methods Appl. Mech. Engrg.*, 195(41-43):5797–5812, 2006.
- [19] S. Deparis, M. Fernandez, and L. Formaggia. Acceleration of a fixed point algorithm for a fluid-structure interaction using transpiration condition. *Math. Model. Numer. Anal.*, 37(4):601–616, 2003.

- [20] J. Donea. *Arbitrary Lagrangian-Eulerian finite element methods*, in: *Computational methods for transient analysis*. North-Holland, Amsterdam, 1983.
- [21] H. Fang, Z. Wang, Z. Lin, and M. Liu. Lattice Boltzmann method for simulating the viscous flow in large distensible blood vessels. *Phys. Rev. E.*, 65(5):051925–1–051925–12, 2002.
- [22] C. Farhat, P. Geuzaine, and C. Grandmont. The discrete geometric conservation law and the nonlinear stability of ale schemes for the solution of flow problems on moving grids. *Journal of Computational Physics*, 174(2):669–694, 2001.
- [23] L.J. Fauci and R. Dillon. Biofluidmechanics of reproduction. In *Annual review of fluid mechanics*. Vol. 38, volume 38 of *Annu. Rev. Fluid Mech.*, pages 371–394. Annual Reviews, Palo Alto, CA, 2006.
- [24] Z.G. Feng and E.E. Michaelides. The immersed boundary-lattice Boltzmann method for solving fluid-particles interaction problems. *J. Comp. Phys.*, 195(2):602–628, 2004.
- [25] M. A. Fernández and M. Moubachir. A newton method using exact jacobians for solving fluid-structure coupling. *Computers and Structures*, 83(2-3):127–142, 2005.
- [26] M.A. Fernández. Incremental displacement-correction schemes for the explicit coupling of a thin structure with an incompressible fluid. *C. R. Math. Acad. Sci. Paris*, 349(7-8):473–477, 2011.
- [27] M.A. Fernández. Incremental displacement-correction schemes for incompressible fluid-structure interaction: stability and convergence analysis. *Numerische Mathematik*, 2012.
- [28] M.A. Fernández, J.F. Gerbeau, and C. Grandmont. A projection algorithm for fluid-structure interaction problems with strong added-mass effect. *Comptes Rendus Mathématique*, 342(4):279–284, 2006.
- [29] M.A. Fernández and J. Mullaert. Displacement-velocity correction schemes for incompressible fluid-structure interaction. *C. R. Math. Acad. Sci. Paris*, 349(17-18):1011–1015, 2011.
- [30] C.A. Figueroa, I.E. Vignon-Clementel, K.E. Jansen, T.J.R. Hughes, and C.A. Taylor. A coupled momentum method for modeling blood

flow in three-dimensional deformable arteries. *Comput. Methods Appl. Mech. Eng.*, 195(41-43):5685–5706, 2006.

- [31] A.L. Fogelson and R.D. Guy. Platelet-wall interactions in continuum models of platelet thrombosis: Formulation and numerical solution. *Math. Med. Biol.*, 21:293–334, 2004.
- [32] L. Formaggia, J.F. Gerbeau, F. Nobile, and A. Quarteroni. On the coupling of 3d and 1d navier-stokes equations for flow problems in compliant vessels. *Comput. Methods Appl. Mech. Eng.*, 191(6-7):561–582, 2001.
- [33] J. Gerbeau and M. Vidrascu. A quasi-newton algorithm based on a reduced model for fluid-structure interactions problems in blood flows. *Math. Model. Numer. Anal.*, 37(4):631–648, 2003.
- [34] R. Glowinski. *Finite element methods for incompressible viscous flow*, in: *P.G.Ciarlet, J.-L.Lions (Eds), Handbook of numerical analysis*, volume 9. North-Holland, Amsterdam, 2003.
- [35] B.E. Griffith. Immersed boundary model of aortic heart valve dynamics with physiological driving and loading conditions. *Int. J. Numer. Methods Biomed. Eng.*, 28(3):317–345, 2012.
- [36] B.E. Griffith. On the volume conservation of the immersed boundary method. *Commun. Comput. Phys.*, 12(2):401–432, 2012.
- [37] B.E. Griffith, R.D. Hornung, D.M. McQueen, and C.S. Peskin. An adaptive, formally second order accurate version of the immersed boundary method. *J. Comput. Phys.*, 223(1):10–49, 2007.
- [38] B.E. Griffith, R. Luo, D.M. McQueen, and C.S. Peskin. Simulating the fluid dynamics of natural and prosthetic heart valves using the immersed boundary method. *Int J Appl Mech.*, 1:137–177, 2009.
- [39] G. Guidoboni, R. Glowinski, N. Cavallini, and S. Čanić. Stable loosely-coupled-type algorithm for fluid-structure interaction in blood flow. *J. Comput. Phys.*, 228(18):6916–6937, 2009.
- [40] S. Hansen and E. Zuazua. Exact controllability and stabilization of a vibrating string with an interior point mass. *SIAM J. Control Optim.*, 33(5):1357–1391, 1995.

- [41] M. Heil. An efficient solver for the fully coupled solution of large-displacement fluid-structure interaction problems. *Comput. Methods Appl. Mech. Eng.*, 193(1-2):1–23, 2004.
- [42] T.J.R. Hughes, W.K. Liu, and T.K. Zimmermann. Lagrangian-eulerian finite element formulation for incompressible viscous flows. *Comput. Methods Appl. Mech. Eng.*, 29(3):329–349, 1981.
- [43] A. Hundertmark-Zaušková, M. Lukáčová-Medvidová, and G. Rusnáková. Fluid-structure interaction for shear-dependent non-Newtonian fluids. In *Topics in mathematical modeling and analysis*, volume 7 of *Jindřich Nečas Cent. Math. Model. Lect. Notes*, pages 109–158. Matfyzpress, Prague, 2012.
- [44] M Koch and E Zuazua. A hybrid system of PDE’s arising in multi-structure interaction: coupling of wave equations in  $n$  and  $n - 1$  space dimensions. Recent trends in partial differential equations, 409 Contemp. Math., Amer. Math. Soc., Providence, RI:55–77, 2006.
- [45] M. Krafczyk, M. Cerrolaza, M. Schulz, and E. Rank. Analysis of 3D transient blood flow passing through an artificial aortic valve by Lattice-Boltzmann methods. *J. Biomech.*, 31(5):453–462, 1998.
- [46] M. Krafczyk, J. Tölke, E. Rank, and M. Schulz. Two-dimensional simulation of fluid-structure interaction using lattice-Boltzmann methods. *Comput. Struct.*, 79(22-25):2031–2037, 2001.
- [47] Young W. Kwon and Angela C. Owens. Dynamic responses of composite structures with fluid- structure interaction. *Advances in Composite Materials - Ecodesign and Analysis*. Ed: B. Attaf, InTech Europe:337–358; ISBN: 978–953–307–150–3, 2011.
- [48] C.S. Peskin L.A. Miller. A computational fluid dynamics study of ‘clap and fling’ in the smallest insects. *J. Exp. Biol.*, 208:195–212, 2005.
- [49] P. Le Tallec and J. Mouro. Fluid structure interaction with large structural displacements. *Comput. Methods Appl. Mech. Eng.*, 190(24-25):3039–3067, 2001.
- [50] V. Lescarret and E. Zuazua. Numerical approximation schemes for multi-dimensional wave equations in asymmetric spaces. *Preprint*.



- [51] A. Leuprecht, K. Perktold, M. Prosi, T. Berk, W. Trubel, and H. Schima. Numerical study of hemodynamics and wall mechanics in distal end-to-side anastomoses of bypass grafts. *J. Biomech.*, 35(2):225–236, 2002.
- [52] S. Lim and C.S. Peskin. Simulations of the whirling instability by the immersed boundary method. *SIAM J. Sci. Comput.*, 25(6):2066–2083, 2004.
- [53] M. Galindo M. Cervera, R. Codina. On the computational efficiency and implementation of block-iterative algorithms for nonlinear coupled problems. *Engrg. Comput.*, 13:4–30, 1996.
- [54] A. Hundertmark-Zaušková M. Lukáčová-Medvid'ová, G. Rusnáková. Kinematic splitting algorithm for fluidstructure interaction in hemodynamics. *Computer Methods in Appl. Mech. Engi.*, To appear., 2013.
- [55] X. Ma, G.C. Lee, and S.G. Lu. Numerical simulation for the propagation of nonlinear pulsatile waves in arteries. *ASME J. Biomech. Eng.*, 114:490–496, 1992.
- [56] H. Matthies and J. Steindorf. Numerical efficiency of different partitioned methods for fluid-structure interaction. *Z. Angew. Math. Mech.*, 2(80):557–558, 2000.
- [57] C Michler, S.J. Hulshoff, E.H. van Brummelen, and R.x de Borst. A monolithic approach to fluid-structure interaction. *Computers and Fluids*, 33:839–848, 2004.
- [58] A. Mikelic, G. Guidoboni, and S. Čanić. Fluid-structure interaction in a pre-stressed tube with thick elastic walls i: the stationary stokes problem. *Networks and Heterogeneous Media*, 2(3):397, 2007.
- [59] L.A. Miller and C.S. Peskin. A computational fluid dynamics of 'clap and fling' in the smallest insects. *J. Exp. Biol.*, 208(2):195–212, 2005.
- [60] B. Muha and title=A nonlinear, 3D fluid-structure interaction problem driven by the time-dependent dynamic pressure data: a constructive existence proof journal=Submitted Canic, S.].
- [61] B. Muha and S. Čanić. Existence of a weak solution to a fluid-structure interaction problem motivated by blood-artery-stent interaction. *In preparation*, 2013.

- [62] B. Muha and S. Čanić. Existence of a Weak Solution to a Nonlinear Fluid–Structure Interaction Problem Modeling the Flow of an Incompressible, Viscous Fluid in a Cylinder with Deformable Walls. *Arch. Ration. Mech. Anal.*, 207(3):919–968, 2013.
- [63] B. Muha and S. Čanić. Existence of a weak solution to a fluid-multi-layered-structure interaction problem. *Journal of Differential Equations*, 256:658–706, 2014.
- [64] C.M. Murea and S. Sy. A fast method for solving fluid-structure interaction problems numerically. *Int. J. Numer. Meth. Fl.*, 60(10):1149–1172, 2009.
- [65] F. Nobile. *Numerical approximation of fluid-structure interaction problems with application to haemodynamics*. PhD thesis, EPFL, Switzerland, 2001.
- [66] F. Nobile and C. Vergara. An effective fluid-structure interaction formulation for vascular dynamics by generalized Robin conditions. *SIAM J. Sci. Comput.*, 30:731–763, 2008.
- [67] C.S. Peskin. Numerical analysis of blood flow in the heart. *J. Computational Phys.*, 25(3):220–252, 1977.
- [68] C.S. Peskin and D.M. McQueen. Modeling prosthetic heart valves for numerical analysis of blood flow in the heart. *J. Comput. Phys.*, 37(1):113–132, 1980.
- [69] A. Quaini and A. Quarteroni. A semi-implicit approach for fluid-structure interaction based on an algebraic fractional step method. *Math. Models Methods Appl. Sci.*, 17(6):957–985, 2007.
- [70] A. Quarteroni, M. Tuveri, and A. Veneziani. Computational vascular fluid dynamics: problems, models and methods. *Comput. Vis. Sci.*, 2(4):163–197, 2000.
- [71] J. Rauch, X. Zhang, and E. Zuazua. Polynomial decay for a hyperbolic-parabolic coupled system. *J. Math. Pures Appl. (9)*, 84(4):407–470, 2005.
- [72] R. Van Loon, P.D. Anderson, J. De Hart, and F.P.T. Baaijens. A combined fictitious domain/adaptive meshing method for fluid-structure interaction in heart valves. *Int. J. Numer. Meth. Fl.*, 46(5):533–544, 2004.

- [73] S. Čanić, D. Lamponi, A. Mikelić, and J. Tambača. Self-consistent effective equations modeling blood flow in medium-to-large compliant arteries. *Multiscale Model. Simul.*, 3(3):559–596, 2005.
- [74] S. Čanić, B. Muha, and M. Bukač. Stability of the kinematically coupled  $\beta$ -scheme for fluid-structure interaction problems in hemodynamics. *Submitted.*, 2012, arXiv:1205.6887.
- [75] Wikipedia. Composite materials. [http://en.wikipedia.org/wiki/Composite\\_material](http://en.wikipedia.org/wiki/Composite_material), 2013.
- [76] X. Zhang and E. Zuazua. Long-time behavior of a coupled heat-wave system arising in fluid-structure interaction. *Arch. Ration. Mech. Anal.*, 184(1):49–120, 2007.
- [77] S. Zhao, X. Xu, and M. Collins. The numerical analysis of fluid-solid interactions for blood flow in arterial structures part 2: development of coupled fluid-solid algorithms. *Proc. Instn. Mech. Eng. Part H*, 212:241–252, 1998.